Interface propagation and microstructure evolution in phase field models of stress-induced martensitic phase transformations

Valery I. Levitas [a,*], Dong-Wook Lee [b,c], Dean L. Preston [d]

[a] *Iowa State University, Departments of Mechanical Engineering, Aerospace Engineering, and Material Science and Engineering, Ames, IA 50011, USA*
[b] *Purdue University, School of Mechanical Engineering, West Lafayette, IN 47907-2088, USA*
[c] *Texas Tech University, Department of Mechanical Engineering, Lubbock, TX 79409-1021, USA*
[d] *Physics Division, Los Alamos National Laboratory, Los Alamos, NM 87545, USA*

ARTICLE INFO

ABSTRACT

Analytical solutions for diffuse interface propagation are found for two recently developed Landau potentials that account for the phenomenology of stress-induced martensitic phase transformations. The solutions include the interface profile and velocity as a function of temperature and stress tensor. An instability in the interface propagation near lattice instability conditions is studied numerically. The effect of material inertia is approximately included. Two methods for introducing an athermal interface friction in phase field models are discussed. In the first method an analytic expression defines the location of the diffuse interface, and the rate of change of the order parameters is required to vanish if the driving force is below a threshold. As an alternative and more physical approach, we demonstrate that the introduction of spatially oscillatory stress fields due to crystal defects and the Peierls barrier, or to a jump in chemical energy, reproduces the effect of an athermal threshold. Finite element simulations of microstructure evolution with and without an athermal threshold are performed. In the presence of spatially oscillatory fields the evolution self-arrests in realistic stationary microstructures, thus the system does not converge to an unphysical single-phase final state, and rate-independent temperature- and stress-induced phase transformation hysteresis are exhibited.

© 2009 Elsevier Ltd. All rights reserved.

1. Introduction

Phase field or Ginzburg–Landau (GL) models are widely used for the simulation of various first-order solid–solid phase transformations; see books Salje (1991) and Toledano and Toledano (1987). In this paper we will focus on martensitic or diffusionless transformations (Ahluwalia et al., 2003; Artemev et al., 2001; Curnoe and Jacobs, 2001a,b; Jacobs et al., 2003; Jin et al., 2001; Levitas and Preston, 2002a,b; Levitas et al., 2003; Levitas and Lee, 2007; Lookman et al., 2003a,b; Rasmussen et al., 2001; Seol et al., 2003; Shenoy et al., 1999; Wang et al., 2001). Deformation of the crystal lattice of the austenite, A, the high-temperature phase, into the martensite, M, the low temperature phase, can be described by the transformation strain tensor $\boldsymbol{\varepsilon}_t$ (also called the Bain strain or spontaneous strain). The relative symmetries of the A and M crystal lattices implies the existence of a finite number n of crystallographically equivalent variants of martensite. All martensitic variants M_i, $i = 1, 2, \ldots, n$, have the same components of the transformation strain tensor in their respective crystallographic bases. A list of components of transformation strain tensors for transformations between various crystal lattices are given, for example, in Bhattacharya (2004) and Pitteri and Zanzotto (2002). The phase field approach describes both stress- and temperature-induced phase transformations in a unified framework.

---

* Corresponding author. Tel.: +1 515 294 9691; fax: +1 801 788 0026.
  E-mail address: vlevitas@iastate.edu (V.I. Levitas).

In the phase field framework the evolution of a multi-connected martensitic microstructure is described by a thermodynamically consistent set of kinetic equations, the Ginzburg–Landau equations, for the order parameters. Order parameters are similar to internal variables in continuum thermodynamics (Valanis, 1996). However, in the phase field approach these internal variables describe material instabilities, such as the instabilities of a crystal lattice responsible for solid–solid phase transformations, twin and dislocation nucleation, melting, fracture and so on. Some theories of martensitic phase transformations employ order parameters related to transformation strains (Artemev et al., 2001; Levitas and Preston, 2002a,b; Levitas et al., 2003; Levitas and Lee, 2007; Seol et al., 2003; Shenoy et al., 1999; Wang and Khachaturyan, 1997; Wang et al., 2001), while the order parameters in other models are the components of the strain tensor responsible for lattice instability (Curnoe and Jacobs, 2001a,b; Jacobs et al., 2003; Lookman et al., 2003a,b; Rasmussen et al., 2001). The thermodynamic (Landau) potential is typically a polynomial in the order parameters with multiple minima (as in Fig. 2) corresponding to the various phases. The phase with the deepest minimum is the stable phase, while other minima correspond to metastable phases; all minima are separated by potential barriers. The thermodynamic potential also includes gradient terms. Solutions of the time-dependent Ginzburg–Landau equation, which describes the evolution of the order parameters, are generally comprised of regions corresponding to local minima of the potential (stable or metastable phases) separated by diffuse stationary or moving interfaces where the gradient energy is localized; it represents the interface energy. The key advantage of the phase field approach is that the computation of the microstructure evolution proceeds without the additional effort required to track multiple interfaces. However, the standard phase field method does not encode the microphysics governing interface propagation.

As we demonstrated in Levitas and Preston (2002a,b), all previous Landau potentials did not account for the typical features of stress–strain curves for martensitic phase transformations, e.g., in shape memory alloys. In our papers (Levitas and Preston, 2002a,b; Levitas et al., 2003) we developed several polynomial Gibbs (Landau) potentials for the description of multivariant stress- and temperature-induced martensitic phase transformations under general three-dimensional loading. These potentials were designed by requiring that they describe the experimentally observed features of martensitic phase transformation in shape memory alloys and steels, specifically, a constant or weakly temperature dependent transformation strain tensor and stress hysteresis, and transformation at non-zero tangent elastic moduli. They include all temperature-dependent thermomechanical properties of the austenite and martensitic variants and describe phase transformations between austenite and martensitic variants and between martensitic variants for arbitrary crystal structures. These potentials are based on order parameters related to transformation strain rather than total strain. We do not know how to derive a similar potential in terms of order parameters related to the total strain.

In Levitas et al. (2003), analytic solutions of the one-dimensional *time-independent* Ginzburg–Landau equations for our 2–3–4 and 2–4–6 polynomial potentials were obtained. Solutions include martensitic (M) and austenitic (A) critical nuclei, and diffuse M–A and M–M interfaces. The widths and energies of the nuclei and interfaces were found as functions of the thermodynamic driving force, the gradient energy coefficient, and a parameter that characterizes the stability of A. Static microstructures in a finite sample, their stabilities, and physical interpretations were studied in Levitas et al. (2006a). Combined surface and size effects and a barrierless nucleation mechanism were analyzed in Levitas et al. (2006b). Dynamic problems were treated in Idesman et al. (2008).

In this paper, interface propagation kinetics is incorporated in the models developed in Levitas and Preston (2002a,b) and Levitas et al. (2003). We consider both one-dimensional (1D) and two-dimensional (2D) cases. In the 1D case, we obtain and analyze both analytical and numerical solutions of the *time-dependent* Ginzburg–Landau equations for both A–M and M–M interface propagation. Both 2–3–4 and 2–4–6 polynomial potentials are used. For the A–M interface an exact solution for the interface profile and velocity is obtained for negligible inertia (mass density), in which case the stress is the same in both A and M, i.e., $\sigma^A = \sigma^M = \sigma$. Analytical relationships between the interface velocity, the driving force for the phase transformation, and a parameter that characterizes the lattice stability of A are obtained and analyzed. For non-zero mass density, $\sigma^A \neq \sigma^M$. To a good approximation the driving force for interface propagation depends on σ^A and σ^M only through their average. Thus, inertial effects can be approximately taken into account by replacing the homogeneous stress σ in the zero-inertia A–M interface solution by $\bar{\sigma} = (\sigma^A + \sigma^M)/2$.

The propagation of M–M and A–M interfaces is studied numerically. For the M–M interface, we simulate the case where the temperature equals the phase equilibrium temperature and an austenitic region appears between the martensitic variants. We present several numerical solutions illustrating instabilities in M–M and A–M interface propagation. When stresses reach and exceed the values corresponding to lattice instability, homogeneous or surface-induced nucleation may occur in addition to interface propagation, and the nucleation interacts with the interface propagation.

In 2D, the coupled Ginzburg–Landau and quasi-static equations of linear elasticity theory are solved using the finite element method (FEM). The coupled evolution of microstructures and stress fields in square samples is studied numerically.

Despite significant success in modeling microstructure formation in Artemev et al. (2001), Curnoe and Jacobs (2001a,b), Jacobs et al. (2003), Jin et al. (2001), Levitas and Preston (2002a,b), Levitas et al. (2003), Levitas and Lee (2007), Lookman et al. (2003a,b), Rasmussen et al. (2001), Seol et al. (2003), Shenoy et al. (1999), Wang and Khachaturyan (1997), and Wang et al. (2001), and here, the phase field approach has a major drawback: it does not include an athermal resistance to interface motion. This resistance is analogous to dry friction in classical mechanics. Because of this athermal resistance, interface propagation occurs only if the driving force for the corresponding phase transformation exceeds a rate-independent threshold *K*. The athermal resistance is responsible for hysteresis in the temperature or the rate-independent part of the stress, and energy dissipation.

In our numerous simulations (some of them are presented below) for a single crystal with homogeneous stresses at the boundary we found that complex martensitic microstructures appear that are similar to those observed experimentally; however, they eventually evolve into a single phase. Similar results have already been reported in the literature (see, for example, Jacobs et al., 2003). Consequently, microstructural formation in samples with stress-free surfaces (temperature-induced phase transformations), with homogeneous stresses at the boundaries (as in the experiments in Abeyaratne et al. (1996)), or with zero stresses at selected surfaces (for example, uniaxial tension–compression or torsion), cannot be modeled. Even for periodic boundary conditions, the final microstructure is sometimes a single variant (Jin et al., 2001; Kerr et al., 1999). In contrast, kinematic constraints, e.g., due to polycrystallinity or prescribed displacements at the boundary, promote stationary multivariant microstructures (Jacobs et al., 2003; Jin et al., 2001; Rasmussen et al., 2001). However, an athermal threshold exists in any case, and if taken into account it would change the microstructure evolution, path dependence, and energetics, especially under cyclic loading. While the necessity of introducing an athermal threshold in phase field modeling has been recognized for a long time, we are not aware of any successful attempts to do so.

An athermal threshold is included in all mesoscale models (Auricchio et al., 2007; Boyd and Lagoudas, 1996; Ghosh and Olson, 1994; Grujicic et al., 1985; Levitas, 1994, 1995, 1998, 2000a,b; Levitas et al., 1999, 2002c; Levitas and Ozsoy, 2009a,b; Lim and McDowell, 2002; Pan et al., 2007; Peng et al., 2008; Thamburaja and Anand, 2002) that include kinetic equations for sharp interfaces or for product phase concentration. It is also included in our recent mesoscale phase field model (Idesman et al., 2005; Levitas et al., 2004) since neglect of the gradient energy term (which is reasonable at the mesoscale) results in a threshold value for the driving force for interface motion. However, the introduction of an athermal threshold in the traditional nanoscale phase field approach (where gradient energy cannot be neglected) is not straightforward because there is no equation for the interface, only evolution equations for the order parameters. Thus, Vedantam (2006) introduced a sophisticated kinetic coefficient in the Ginzburg–Landau equation that is singular for zero rate of change of the order parameter $\dot{\eta}$, which allows one to obtain $\dot{\eta} = 0$ for non-zero driving force. However, the introduction of such a threshold in the kinetic equation for the order parameters arrests certain unphysical intermediate configurations (e.g., particular critical nuclei); therefore the system does not converge to a realistic microstructure consisting of austenite A and martensitic variants M_i divided by moving or fixed diffuse interfaces. Note that a similar problem exists in the phase field theory of dislocations (Hu et al., 2004; Wang et al., 2001). In Wang et al. (2001), a periodic thermodynamic potential in terms of *order parameters* was introduced for dislocations. The potential, which was called a 'Peierls potential', was supposed to represent the Peierls barrier to interface propagation due to discreteness of the crystal lattice, but it was shown in Hu et al. (2004) using an analytical solution for the dislocation that there was in fact no athermal threshold. Similarly, the analytical expressions for interface velocity in our original GL model (Levitas and Preston, 2002a,b; Levitas et al., 2003) do not include an athermal threshold. More generally, there is no threshold in any GL model because the gradient energy term renders it non-local, thus interface points are coupled through the order parameter and interface motion occurs at any non-zero driving force. Since there is no essential difference between GL theories for phase transformations or dislocations, a prescription for introducing an athermal threshold for interface motion applies equally well to dislocations.

An athermal threshold appears in phase field theory when the latent heat of transformation is taken into account (Ngan and Truskinovsky, 1999). Allowance for microinertia related to the strain tensor also produces a threshold (Theil and Levitas, 2000). A discrete model can exhibit athermal hysteresis; see Kressea and Truskinovsky (2003). The quasi-continuum approximation of a discrete model can also exhibit some hysteresis, but it is much smaller than for the initial discrete model (Kressea and Truskinovsky, 2003).

None of the above approaches solves the problem of athermal friction for interfaces or dislocations. Indeed, for slow interface motion, the hysteresis due to latent heat release or internal inertia is too small to account for measured values of K. In fact, apart from the Peierls barrier, the origin of the athermal threshold K is the interaction of the moving interface or dislocations with the long-range stress fields of point and line defects, and various boundaries (e.g., twin and tilt boundaries) (Ghosh and Olson, 1994; Grujicic et al., 1985; Kocks et al., 1975). The most compelling evidence to support this claim is the observed proportionality of the athermal threshold and the rate-independent hysteresis to the yield strength, which characterizes the types, densities, and distributions of the point, line, and boundary defects that limit dislocation motion; see Levitas (1997, 1998, 2004) for high pressure phase transformations, and Ghosh and Olson (1994) and Levitas et al. (2002c) for martensitic transformations in steel. Also, it is known that the phase transformation hysteresis is changed along with the defect microstructure by thermomechanical treatment (Hornbogen, 1999).

In this paper, we propose two different schemes for introducing an athermal interface friction in phase field models, and we show that each provides a realistic description of interface propagation. In the first method, an analytic expression defines the location of the diffuse interface, and the rate of change of the order parameters in a neighborhood of the interface is required to vanish if the driving force is below some threshold. In that case, the interface is subject to an athermal friction similar to that experienced by sharp interfaces in micromechanical models, and the value of K is the only required information. This method works well in the 1D case but should be checked for 2D and 3D problems. As an alternative approach, we demonstrate that the introduction in our phase field model of spatially oscillatory stress fields (due to the Peierls barrier and various defects), or of a jump in chemical energy, ΔG^0, reproduces the effect of an athermal threshold on interface propagation. In the presence of spatially oscillatory fields, experimentally observed microstructures self-arrest before the system can converge to a single-phase final state, and rate-independent temperature- and stress-induced phase transformation hysteresis are exhibited. These fields do not affect the evolution of an intermediate microstructure, such as a critical nucleus, to an $A—M_i$ or $M_i—M_j$ microstructure divided by diffuse interfaces. Also, some experimentally observed microstructures appear in phase field simulations with

oscillatory fields that do not follow from GL energy minimization. A similar approach can be applied to other phase transformations – reconstructive, ferroelectric, ferroelastic, and magnetoelastic – as well as to dislocation motion. The incorporation of spatially oscillatory fields in phase field models dramatically improves the fidelity of numerical simulations of the development of martensitic microstructures. However, a new problem arises: the necessity of finding realistic oscillatory fields corresponding to a given defect structure; this is just as important but even more challenging than finding a proper Landau potential. We also discuss the introduction of an athermal threshold in a model for thermally activated dislocation motion. The results of many FEM simulations of microstructure evolution with an athermal barrier are presented.

Note that, practically speaking, the phase field approach is limited to nanoscale samples because the width of the diffuse interface is of the order of magnitude of 1 nm and it has to be resolved with several finite elements. In the given paper, all material parameters for the thermodynamic potential were determined from the results of molecular dynamic simulations (see Levitas and Preston, 2002b). At such small scales (for example, in nanofilms), one usually neglects nucleating crystal defects. Then, there are no stress concentrators to promote nucleation, and nucleation occurs close to the lattice instability at stresses of the order of magnitude of 10 GPa. These values correspond to molecular dynamic simulations while stresses measured in macroscopic experiments are below 1 GPa. This situation is similar to the case of fracture and/or plastic flow: stresses that cause fracture and plastic flow in defect-free nanoscale volumes correspond to the theoretical strength, which is of the order of magnitude of 10 GPA; the engineering strength and yield strength for materials with defects are 1–2 orders of magnitude lower. In contrast, interface propagation can occur close to the thermodynamic equilibrium conditions, and we operate with stresses of several 100 MPa.

Some authors (e.g., Vedantam, 2006) calibrate the parameters in the thermodynamic potential using experimental data for macroscopic samples. With these parameter values, interface widths and energies are calculated to have values much larger than those observed. The problem is that the parameter values determined from macroscopic data incorporate the effects of mesoscale defects and should not be used at small length scales. The microscale phase field approach is based on essentially different concepts (see Levitas et al., 2004; Idesman et al., 2005).

2. Interface propagation in one dimension

In this section we provide the background and establish notation for our analytical and numerical studies of A–M and M–M interface propagation in one dimension. All transformations can be described with a single order parameter. The order parameter, η, is a function of the coordinate x in the direction of propagation $\mathbf{n}$; $\mathbf{n} \cdot \mathbf{n} = 1$. Numerical simulations are carried out in a rectangular parallelepiped in an arbitrary three-dimensional homogeneous stress field $\boldsymbol{\sigma}$; the corresponding normal and shear stresses on the surface are denoted σ_i $(i = 1, 2)$ and τ (Fig. 1). The transformation strain which transforms the crystal lattice of A into the lattice of M is the invariant plane strain $\boldsymbol{\varepsilon}_t = \frac{1}{2}\gamma(\mathbf{mn} + \mathbf{nm})\,sign(\eta) + \varepsilon\mathbf{nn}$, where γ is the shear strain in direction $\mathbf{m}$ in the habit plane with normal $\mathbf{n}$ (direction of interface propagation) and normal strain ε along $\mathbf{n}$; the faces of the parallelepiped are orthogonal and parallel to $\mathbf{n}$ and $\mathbf{m}$. The transformation strain as a function of order parameter is described by the following equations:

$$\bar{\varepsilon}_{t6} = \varepsilon_t \varphi_6(\eta) \quad \text{and} \quad \bar{\varepsilon}_{t4} = \varepsilon_t \varphi_4(\eta), \tag{1}$$
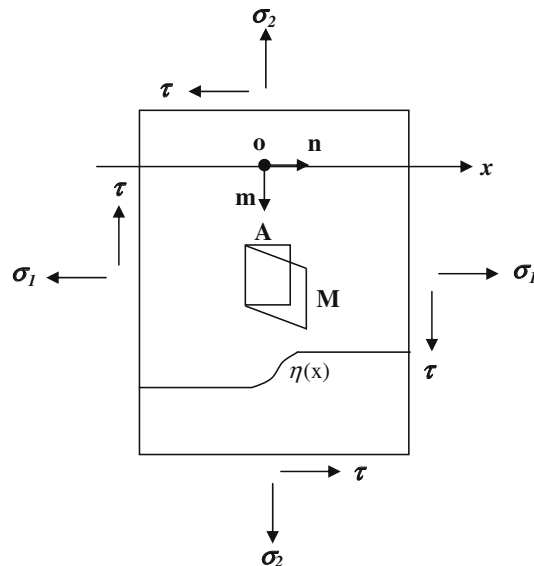

Fig. 1. Schematic of solution of the Landau–Ginzburg equation in 1D. The curve labled $\eta(x)$ represents the solution. The crystal lattice transforms from austenite to martensite by an invariant plane strain.

where

$$\varphi_6(\eta) = a\eta^2/2 + (3-a)\eta^4 + (a-4)\eta^6/2 \quad \text{and} \quad \varphi_4(\eta) = a\eta^2 + (4-2a)\eta^3 + (a-3)\eta^4, \tag{2}$$

and a is a material parameter, $0 \leqslant a \leqslant 6$. Here and later the subscripts 4 and 6 refer to the 2–3–4 and 2–4–6 potentials, respectively. The 2–4–6 and 2–3–4 potentials derived in Levitas et al. (2003) are

$$G_6 = s_1\eta^2[1 - (4-P)\eta^2/2 + (3-P)\eta^4/3]/2, \tag{3}$$

$$G_4 = s_1\eta^2[1 - (6-P)\eta/3 + (4-P)\eta^2/4], \tag{4}$$

$$s_1 := A - a\boldsymbol{\sigma} : \boldsymbol{\varepsilon}_t, \quad s_2 := 12(\Delta G^\theta - \boldsymbol{\sigma} : \boldsymbol{\varepsilon}_t), \quad P := s_2/s_1. \tag{5}$$

The order parameter satisfies $-1 \leqslant \eta \leqslant 1$ for the 2–4–6 potential and $0 \leqslant \eta \leqslant 1$ for the 2–3–4 potential. ΔG^θ is the difference between the thermal parts of the Gibbs energies of M and A. Note that elastic strains are neglected in Eqs. (3)–(5), but can be trivially included. The minima of the potential G_4 are at $\eta = 0$ (A), $\eta = 1$ (M), and for G_6 the minima are at $\eta = 0$ (A), $\eta = 1$ (M$_+$), $\eta = -1$ (M$_-$), independent of $\boldsymbol{\sigma}$ and temperature θ (Fig. 2). The quantity s_1 characterizes the stability of the austenite lattice; $s_1 = 0$ corresponds to the loss of A lattice stability, i.e., to the disappearance of the A minimum. For both potentials, the thermodynamic driving force for the M → A transition, i.e., $G(1)-G(0)$, is equal to $s_2/12$. However, the rate of the M → A transformation is controlled not just by the driving force but also by the height of the potential barrier separating the A and M minima. The location and height of this barrier are simple rational functions of s_1 and s_2; in the limit $s_2 \to 0$ of small driving force the barrier height is $G_4 = (1/16)s_1$, $G_6 = (2/27)s_1$.

Adding a gradient energy term to the Landau free energy yields the Ginzburg–Landau energy $\tilde{G}_{GL} = G + \boldsymbol{\beta}(d\boldsymbol{\eta}/dx)^2$ and $G_{GL} = \int_l \tilde{G}_{GL}dx$. The time-dependent Ginzburg–Landau (TDGL) equation follows from the assumption that the generalized flux $\partial\eta/\partial t$ is proportional to the generalized force $-\delta G_{GL}/\delta\eta$:

$$\frac{\partial\eta}{\partial t} = -\lambda\frac{\delta G_{GL}}{\delta\eta} = -\lambda\left(\frac{\partial G}{\partial\eta} - 2\beta\frac{\partial^2\eta}{\partial x^2}\right). \tag{6}$$

Here $\delta G_{GL}/\delta\eta$ is the functional derivative of G_{GL} with respect to η; $\lambda > 0$ and $\beta > 0$ are the kinetic and gradient energy coefficients with dimensions of *volume/energy–time* and *energy/length*, respectively. The GL equation for the 2–3–4 potential can be written

$$\frac{\partial\eta}{\partial t'} = \frac{\partial^2\eta}{\partial x'^2} - \eta(\eta-1)\left(\eta - \frac{2s_1}{4s_1 - s_2}\right),$$
$$t' = (4s_1 - s_2)\lambda t, \quad x' = \sqrt{\frac{4s_1 - s_2}{2\beta}}x, \tag{7}$$

and the GL equation for the 2–4–6 potential is

$$\frac{\partial\eta}{\partial t'} = \frac{\partial^2\eta}{\partial x'^2} - \eta(\eta^2-1)\left(\eta^2 - \frac{s_1}{3s_1 - s_2}\right),$$
$$t' = (3s_1 - s_2)\lambda t, \quad x' = \sqrt{\frac{3s_1 - s_2}{2\beta}}x. \tag{8}$$

Note that Eqs. (7) and (8) are nonlinear diffusion equations, and as such possess solitonic solutions representing propagating interfaces.
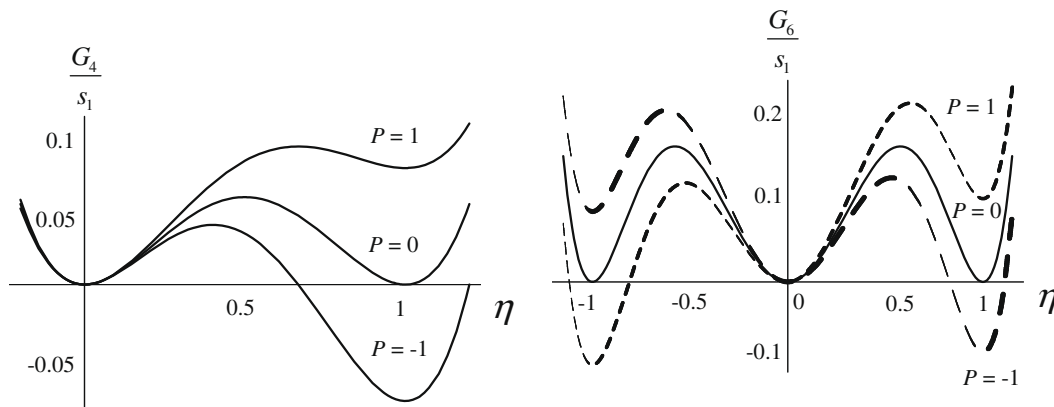

Fig. 2. Plot of Landau potential versus order parameter for the potentials G_4 and G_6.

The equations of motion read

$$\frac{\partial \sigma}{\partial x} = \rho \frac{\partial^2 u}{\partial t^2}, \quad \frac{\partial \tau}{\partial x} = \rho \frac{\partial^2 v}{\partial t^2}, \tag{9}$$

where ρ is the mass density, u and v are the displacements in the directions $\mathbf{n}$ and $\mathbf{m}$, respectively, $\sigma = \mathbf{n} \cdot \boldsymbol{\sigma} \cdot \mathbf{n}$ is the normal stress ($\sigma = \sigma_1$ in Fig. 1) and $\tau = \mathbf{n} \cdot \boldsymbol{\sigma} \cdot \mathbf{m}$ is the shear stress; it follows that $\boldsymbol{\sigma} : \boldsymbol{\varepsilon}_t = \sigma \varepsilon + \tau \gamma \, sign(\eta)$.

3. Analytical kink solutions: propagating A–M diffuse interfaces

3.1. Zero inertia

3.1.1. Interface profile
The neglect of inertia (mass density) in the equations of motion, Eq. (9) means that the stresses σ and τ are constants; hence, $s_1 = A - a[\sigma \varepsilon + \tau \gamma \, sign(\eta)]$ and $s_2 = \Delta G^\theta - \sigma \varepsilon - \tau \gamma \, sign(\eta)$ are nearly constant provided the temperature change accompanying the phase transformation is small. We consider the case where the phase is A as $x \to -\infty$ and M as $x \to +\infty$. When A and M are in thermodynamic equilibrium, then, $G(-\infty) = G(A) = G(+\infty) = G(M) = 0$ and $s_2 = P = 0$. The solutions of the static version of Eq. (6) read (Levitas et al., 2003)

$$\eta_{4s}^{AM}(x) = \left[1 + \exp\left(-\sqrt{s_1/\beta}(x - x_0) \right) \right]^{-1}, \quad \eta_{6s}^{AM}(x) = \left[1 + \exp\left(-\sqrt{2s_1/\beta}(x - x_0) \right) \right]^{-1/2}. \tag{10}$$

The transformation strain profiles $\varphi_4[\eta(x)]$ and $\varphi_6[\eta(x)]$ and the $\eta(x)$ profiles are shown in Fig. 13 in Levitas et al. (2003) and schematically in Fig. 1. They smoothly connect the austenitic ($\eta = 0$) and martensitic ($\eta = 1$) regions.

Propagating interface solutions of the TDGL equation, Eq. (6), for our 2–3–4 and 2–4–6 potentials for constant stresses σ and τ (zero mass density in the equations of motion, Eq. (9)) can be obtained by generalizing the forms of η_{4s}^{AM} and η_{6s}^{AM} given in Eq. (10). In the case of the 2–3–4 potential we write

$$\eta_4^{AM}(\zeta) = \left[1 + \exp\left(-\sqrt{s_1/\beta}\zeta + F(\zeta) \right) \right]^{-1}, \quad \zeta = x - c_4 t. \tag{11}$$

Here c_4 is the interface velocity and F is a function to be determined. Substituting Eq. (11) in Eq. (6) and requiring the coefficients of powers of $\exp(-\sqrt{s_1/\beta}\zeta)$ and $\exp(F(\zeta))$ to vanish, one obtains simultaneous equations for $dF/d\zeta$ and $dF^2/d\zeta^2$. These equations are quadratic in $dF/d\zeta$; signs are chosen so that $cs_2 > 0$ (i.e., when $c < 0$ and the M phase grows to the left, then $s_2 < 0$) and $dF/d\zeta = 0$ for $s_2 = 0$. The F derivatives are given by

$$dF/d\zeta = \sqrt{\frac{s_1}{\beta}} - \frac{\sqrt{4s_1 - s_2}}{2\sqrt{\beta}}, \quad dF^2/d\zeta^2 = \frac{\frac{c_4\sqrt{4s_1 - s_2}}{\beta^{3/2}} - \frac{\lambda s_2}{\beta}}{4\lambda}. \tag{12}$$

Since $dF/d\zeta$ is constant, then $dF^2/d\zeta^2 = 0$, which determines the interface velocity c_4. Finally, we obtain

$$\eta_4^{AM}(x, t) = \frac{1}{1 + e^{-\frac{\sqrt{4s_1 - s_2}}{2\sqrt{\beta}}(x - c_4 t)}}, \quad c_4 = \frac{\lambda s_2 \sqrt{\beta}}{\sqrt{4s_1 - s_2}} = \lambda \sqrt{\beta \alpha s_2} \, sign(s_2), \tag{13}$$

where $\alpha := P/(4 - P) = s_2/(4s_1 - s_2)$ ($\alpha = 0$ for thermodynamic equilibrium, $\alpha = 1$ when M loses its stability, and $\alpha = -1$ when A loses its stability). For the 2–4–6 potential we have

$$\eta_6^{AM}(x, t) = \frac{1}{\sqrt{1 + e^{-\sqrt{\frac{6s_1 - 2s_2}{3\beta}}(x - c_6 t)}}}, \quad c_6 = \sqrt{\frac{2\beta}{3}} \frac{\lambda s_2}{\sqrt{3s_1 - s_2}} = \frac{2}{\sqrt{3}} \frac{\lambda \sqrt{2\beta \alpha s_2}}{\sqrt{3 - \alpha}} \, sign(s_2). \tag{14}$$

3.1.2. Interface velocity
In contrast to the sharp interface approximation in which the interface velocity depends only on the driving force for the phase transformation, in the phase field approach there is also an explicit dependence on s_1 (or α) which characterizes the relative stabilities of the phases. However, in Eq. (13) for c_4, s_1 appears only in the combination

$$4s_1 - s_2 = 4(A(\theta) - a\boldsymbol{\sigma} : \boldsymbol{\varepsilon}_t) - 12\left(\Delta G^\theta - \boldsymbol{\sigma} : \boldsymbol{\varepsilon}_t \right), \tag{15}$$

though in Eq. (14) for c_6, s_1 appears in the combination $3s_1 - s_2 = (3/4)(4s_1 - s_2) - s_2/4$. Using the approximate relations (Levitas and Preston, 2002a,b)

$$A = A_0(\theta - \theta_c), \quad \Delta G^\theta = A_0(\theta - \theta_e)/3, \tag{16}$$

where θ_e is the equilibrium temperature for stress-free A and M, θ_c is the temperature of A loss of stability for zero stress, and $A_0 = -3\Delta s$ with Δs for transformation entropy, we find

$$4s_1 - s_2 = A_0(\theta_e - \theta_c) + (3 - a)\boldsymbol{\sigma} : \boldsymbol{\varepsilon}_t. \tag{17}$$

Remarkably, the temperature dependencies of $A(\theta)$ and G^θ have cancelled, and since a is approximately equal to 3 (Levitas and Preston, 2002a,b), we set $a = 3$, thereby eliminating the dependence on stress as well; therefore

$$4s_1 - s_2 = A_0(\theta_e - \theta_c) \equiv \widetilde{A} \tag{18}$$

is a constant. With these approximations it follows that α and the interface velocities in both potentials are functions of only the driving force, as in the sharp interface approximation

$$\alpha = \frac{s_2}{4\widetilde{A}}, \quad c_4 = \frac{\lambda s_2 \sqrt{\beta}}{2\sqrt{\widetilde{A}}}, \quad c_6 = \frac{2\lambda s_2 \sqrt{2\beta}}{\sqrt{3}\sqrt{12\widetilde{A} - s_2}}. \tag{19}$$

In this approximation, α is proportional to s_2 and has no additional dependency on stresses. For the 2–3–4 potential, the interface velocity is proportional to the driving force for the phase transformation, but for the 2–4–6 potential the dependence is nonlinear: it is stronger than linear for M $\rightarrow$ A phase transformation and weaker than linear for A $\rightarrow$ M phase transformation.

3.1.3. Interface width
The AM interface width is defined in Levitas et al. (2003) by

$$\Delta^{AM} := \left(\frac{d\varphi[\eta(\zeta)]}{d\zeta}\right)_{max}^{-1}, \tag{20}$$

which results in

$$\begin{aligned}
\Delta_4^{AM} &= \frac{2(21 - 5a + Y_4)^5}{32(a - 6)^3(11a^3 - 81(9 + Y_4) - 5a^2(24 + Y_4) + a(486 + 39Y_4))}\sqrt{\frac{\beta}{4s_1 - s_2}}, \\
\Delta_6^{AM} &= \frac{(72 - 15a + Y_6)^4}{128\sqrt{2}(a - 6)^3(-27a^2 - 24(24 + Y_6) + 5a(48 + Y_6))}\sqrt{\frac{3\beta}{3s_1 - s_2}}, \\
Y_4 &:= \sqrt{81 - 30a + 5a^2}, \quad Y_6 := \sqrt{576 - 240a + 33a^2}.
\end{aligned} \tag{21}$$

Both Δ_4^{AM} and Δ_6^{AM} are complicated functions of a but they are accurately approximated by the polynomials

$$\begin{aligned}
1.88 &\leqslant p_6(a) = 1.88 + 0.179a + 0.00065a^2 - 0.0035a^3 \leqslant 2.386, \\
4.822 &\leqslant p_4(a) = -0.056(a - 3)^2 + 5.334 \leqslant 5.334.
\end{aligned} \tag{22}$$

Then we obtain

$$\Delta_4^{AM} = p_4(a)\sqrt{\frac{\beta}{4s_1 - s_2}} = p_4(a)\sqrt{\frac{\beta\alpha}{s_2}}, \quad \Delta_6^{AM} = p_6(a)\sqrt{\frac{3\beta}{3s_1 - s_2}} = 2p_6(a)\sqrt{\frac{3\beta\alpha}{(3 - \alpha)s_2}}. \tag{23}$$

In the approximation of Eq. (19)

$$\Delta_4^{AM} = 2.668\sqrt{\frac{\beta}{\widetilde{A}}}, \quad \Delta_6^{AM} = 8.066\sqrt{\frac{\beta}{12\widetilde{A} - s_2}}. \tag{24}$$

The interface thickness for the 2–3–4 potential is independent of the driving force, but for the 2–4–6 potential it increases (decreases) with driving force for the M $\rightarrow$ A (A $\rightarrow$ M) phase transformation.

3.1.4. Evaluation of λ
To obtain an order of magnitude estimate of the kinetic coefficient λ we take $a = 3$ and $s_1 = 0$ (loss of A stability), for which $s_2 = -4\widetilde{A}$, and approximate the interface velocity by the shear wave velocity c_s. From Eq. (19) we obtain

$$c_s = 2\lambda_4\sqrt{\beta\widetilde{A}} = 2\lambda_6\sqrt{2\beta\widetilde{A}/3}. \tag{25}$$

Using the following data for NiAl (Levitas and Preston, 2002a,b; Levitas et al., 2003; Miracle, 1993)

$$\begin{aligned}
A_0 &= 4.40\,\text{MPa K}^{-1}, \quad \beta = 2.59 \times 10^{-10}\,\text{N}, \quad \theta_e = 215\,\text{K}, \quad \theta_c = -183\,\text{K}, \quad \rho = 5850\,\text{kg/m}^3, \\
G &= 71.5\,\text{GPa}, \quad \text{and} \quad c_s = \sqrt{G/\rho} = 3496\,\text{m/s},
\end{aligned} \tag{26}$$

we obtain

$$\lambda_4 = \sqrt{2/3}\lambda_6 = 2596 \text{ m}^2/\text{N s}. \tag{27}$$

Note that $\beta = 2.59 \times 10^{-10}$ N corresponds to the equilibrium width of 1 nm for a M–M interface (Levitas and Preston, 2002a,b; Levitas et al., 2003). For a M–M interface width of 0.3 nm (which corresponds to an interatomic distance) the gradient energy and kinetic coefficients are respectively decreased and increased to

$$\beta = 2.33 \times 10^{-11}N \quad \text{and} \quad \lambda_4 = \lambda_6/\sqrt{3} = 8653.5 \text{ m}^2/\text{N s}. \tag{28}$$

3.2. Inertial effects on interface propagation

The results of the previous section are valid in the limit of zero mass density, which implies constant stresses σ and τ. The actual stress variation and the corresponding solutions for η are governed by the coupled equations of elasticity theory and Eqs. (6) and (9). An analytic solution is impossible, so we have developed an approximation scheme.

We consider a diffuse planar interface separating A at $x \to -\infty$ from M at $x \to +\infty$; the unit normal to this plane, **n**, is directed from A to M. The stress tensor $\boldsymbol{\sigma}$, which has the normal component σ and in-plane shear component τ, varies from $\boldsymbol{\sigma}^A$ at $x \to -\infty$ to the prescribed value $\boldsymbol{\sigma}^M$ at $x \to \infty$.

The driving force for M $\to$ A is $s_2/12 = \Delta G^\theta - \boldsymbol{\sigma} : \boldsymbol{\varepsilon}_t$, where $\boldsymbol{\sigma} : \boldsymbol{\varepsilon}_t$ is the transformation work per unit volume. Consider an interface separating A at $-\infty$ from M at $+\infty$ that is propagating at constant speed $+c$. The transformation work is obtained by integration

$$W_t = \int_{-\infty}^{\infty} d\zeta \, \boldsymbol{\sigma} : \frac{d\boldsymbol{\varepsilon}_t}{d\zeta}, \tag{29}$$

where $\zeta = x - ct$. We define interface profiles f_σ and f_ϵ for the stress and transformation strain

$$\boldsymbol{\sigma}(\zeta) = \boldsymbol{\sigma}^M + (\boldsymbol{\sigma}^A - \boldsymbol{\sigma}^M) f_\sigma(\zeta),$$
$$\boldsymbol{\varepsilon}_t(\zeta) = \boldsymbol{\varepsilon}_t f_\epsilon(\zeta). \tag{30}$$

The profiles satisfy $f_{\sigma,\epsilon} \sim 1$ for $\zeta \to +\infty$ and $f_{\sigma,\epsilon} \sim 0$ for $\zeta \to -\infty$. If $f_\sigma = f_\epsilon$ then the transformation work is independent of the profile

$$W_t = \frac{1}{2}(\boldsymbol{\sigma}^A + \boldsymbol{\sigma}^M) : \boldsymbol{\varepsilon}_t, \tag{31}$$

but in general $f_\sigma \neq f_\epsilon$. In this case we approximate the profiles by quartic polynomials constrained to satisfy $f_{\sigma,\epsilon}(0) = 0$ and $f_{\sigma,\epsilon}(\zeta_0) = 1$ (ζ_0 is the interface thickness), and $f'_{\sigma,\epsilon}(0) = f'_{\sigma,\epsilon}(\zeta_0) = 0$. The resulting one-parameter interface profiles are

$$f_{\sigma,\epsilon}(\zeta) = \alpha_{\sigma,\epsilon}(\zeta/\zeta_0)^2 + (4 - 2\alpha_{\sigma,\epsilon})(\zeta/\zeta_0)^3 + (\alpha_{\sigma,\epsilon} - 3)(\zeta/\zeta_0)^4 \tag{32}$$

which is just $\varphi_4(\zeta/\zeta_0)$ with a replaced by $\alpha_{\sigma,\epsilon}$. The transformation work is

$$W_t = \frac{1}{2}(\boldsymbol{\sigma}^A + \boldsymbol{\sigma}^M) : \boldsymbol{\varepsilon}_t + \frac{3}{35}(\alpha_\sigma - \alpha_\epsilon) \cdot \frac{1}{2}(\boldsymbol{\sigma}^A - \boldsymbol{\sigma}^M) : \boldsymbol{\varepsilon}_t. \tag{33}$$

Note that W_t is independent of the interface thickness. The contribution of $(1/2)(\boldsymbol{\sigma}^A - \boldsymbol{\sigma}^M) : \boldsymbol{\varepsilon}_t$ to W_t, which arises from the difference between the stress and strain profiles, is suppressed by roughly an order of magnitude (3/35) relative to $(1/2)(\boldsymbol{\sigma}^A + \boldsymbol{\sigma}^M) : \boldsymbol{\varepsilon}_t$. To a good approximation, W_t, and therefore the driving force depends on the stresses in the A and M only through their average: $\bar{\boldsymbol{\sigma}} := (\boldsymbol{\sigma}^A + \boldsymbol{\sigma}^M)/2$; hence, $W_t = \bar{\boldsymbol{\sigma}} : \boldsymbol{\varepsilon}_t$. Thus, in this approximation, inertial (finite mass density) effects are taken into account by replacing the constant stress $\boldsymbol{\sigma}$ by $\bar{\boldsymbol{\sigma}}$. This is consistent with the sharp interface approach (Abeyaratne and Knowles, 1993; Kondaurov and Nikitin, 1986). Accordingly, we utilize Eqs. (13) and (14) with $\boldsymbol{\sigma} \to \bar{\boldsymbol{\sigma}}$ for the general dynamic case.

Combining the Hadamard compatibility condition $[\mathbf{v}] = -c[\mathbf{F}] \cdot \mathbf{n}$ with the jump condition $(\boldsymbol{\sigma}^M - \boldsymbol{\sigma}^A) \cdot \mathbf{n} = -\rho c[\mathbf{v}]$ corresponding to the equation of motion (9), one obtains for sharp interface

$$(\boldsymbol{\sigma}^M - \boldsymbol{\sigma}^A) \cdot \mathbf{n} = \rho c^2 [\mathbf{F}] \cdot \mathbf{n}. \tag{34}$$

Here $[\mathbf{a}] = \mathbf{a}^M - \mathbf{a}^A$, **v** is the particle velocity, and **F** is the deformation gradient. Neglecting the jump in elastic strain across the interface, one obtains $[\mathbf{F}] = \gamma\mathbf{mn} + \varepsilon\mathbf{nn}$ for invariant plane strain. Then Eq. (34) reads

$$\sigma^M - \sigma^A = \rho c^2 \varepsilon, \quad \tau^M - \tau^A = \rho c^2 \gamma. \tag{35}$$

In the definitions of s_1 and s_2, $\bar{\boldsymbol{\sigma}} : \boldsymbol{\varepsilon}_t = \bar{\sigma}\varepsilon + \bar{\tau}\gamma$. Considering σ^M and τ^M as prescribed values, Eqs. (35) and (13)$_2$ (or Eq. (14)$_2$) constitute three equations in the three unknowns σ^A, τ^A (or equivalently $\bar{\sigma}$ and $\bar{\tau}$), and c. The solutions for both potentials are given by

$$\bar{\sigma} = \frac{Z_4\sigma^M - \gamma\varepsilon Z_3\tau^M - \varepsilon Z_7}{2(\gamma^2 + \varepsilon^2)Z_1}, \quad \bar{\tau} = \frac{Z_5\tau^M - \gamma\varepsilon Z_3\sigma^M - \gamma Z_7}{2(\gamma^2 + \varepsilon^2)Z_1}, \tag{36}$$

$$c^2 = \frac{Z_3(\varepsilon\sigma^M + \gamma\tau^M) + Z_7}{\rho(\gamma^2 + \varepsilon^2)Z_1}, \tag{37}$$

with

$$
\begin{aligned}
&Z_1 = m\beta(\gamma^2 + \varepsilon^2)\lambda^2\rho, \quad Z_2 = n - a + Z_1, \quad Z_3 = n - a + 2Z_1, \\
&Z_4 = (n-3)(2\gamma^2 + \varepsilon^2) + 2\gamma^2 Z_1, \quad Z_5 = (n-3)(\gamma^2 + 2\varepsilon^2) + 2\varepsilon^2 Z_1, \quad Z_6 = A - \Delta G^\theta(n + 2Z_1), \\
&Z_7 = Z_6 - \left(\left[Z_6 + Z_3(\varepsilon\sigma^M + \gamma\tau^M)\right]^2 - 4Z_1 Z_2\left(\varepsilon\sigma^M + \gamma\tau^M - \Delta G^\theta\right)^2 \right)^{1/2},
\end{aligned}
\tag{38}
$$

where $(m, n) = (18, 3)$ for the 2–3–4 potential and $(m, n) = (16, 4)$ for the 2–4–6 potential. The sign of c is chosen from the condition $cs_2 > 0$, i.e that the stable phase grows. To choose the physically relevant solution when solving the quadratic we require $\bar{\sigma} = \sigma^M$ and $\bar{\tau} = \tau^M$ in the limit of zero inertia ($\rho = 0$). The above equations describe the propagation of a diffuse interface with approximate allowance for stress variation across the interface. In thermodynamic equilibrium, $s_2 = 0$, and Eq. (36) reduces to $\bar{\sigma} = \sigma^M$ and $\bar{\tau} = \tau^M$.

The dependence of $\sigma^M - \bar{\sigma}$ on σ^M for several values of τ^M is presented in Fig. 3. Despite significant differences between the 2–3–4 and 2–4–6 potentials, the $\sigma^M - \bar{\sigma}$ versus σ^M curves for the two potentials nearly coincide. The corresponding relation between interface velocity and σ^M for the 2–3–4 potential, determined with the help of Eq. (13) (for $\bar{\sigma} = \sigma^M$) and (37) is shown in Fig. 4. In addition to the parameter values for NiAl from Eq. (26), we also used the values $\gamma = 0.2$, $\varepsilon = 0.1$, and $\theta = 300$ K for Figs. 3 and 4.

4. Numerical study: propagation and stability of A–M, M–M, and M–A–M interfaces

In this section we present the results of FEM simulations of A–M and M–M interface propagation, interactions between interfaces, and the stability of interface propagation. Introducing the dimensionless parameters

$$\bar{G}_{GL} = \tilde{G}_{GL}/\tilde{A}, \quad \bar{x} = x\sqrt{\frac{\tilde{A}}{\beta}}, \quad \bar{t} = t\lambda\tilde{A} \tag{39}$$

where $\tilde{A} = A_0(\theta_e - \theta_c)$ (defined in Eq. (18)), we obtain

$$\frac{\partial\eta}{\partial\bar{t}} = -\frac{\delta\bar{G}_{GL}}{\delta\eta} = -\left(\frac{\partial\bar{G}}{\partial\eta} - 2\frac{\partial^2\eta}{\partial\bar{x}^2}\right). \tag{40}$$

We use boundary conditions at the ends of the sample corresponding to equal surface energies of A and M:

$$\frac{d\eta(-l/2)}{dx} = \frac{d\eta(l/2)}{dx} = 0, \tag{41}$$

where l is the sample length. The material parameters are those of NiAl given in Eq. (26); in addition, we have used $a = 2.98$. The temperature is fixed at $\theta = \theta_e$; the driving force for phase transformation is varied by changing the stress σ.
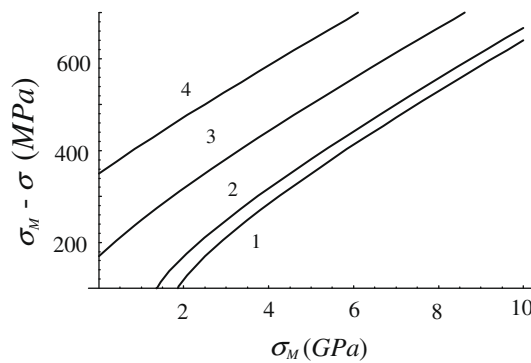

Fig. 3. Dependence of $\sigma_M - \sigma$ on σ_M for four values of the shear stress τ for the 2–3–4 potential: (1) $\tau = 0$; (2) $\tau = 100$ MPa; (3) $\tau = 500$ MPa; (4) $\tau = 1000$ MPa.
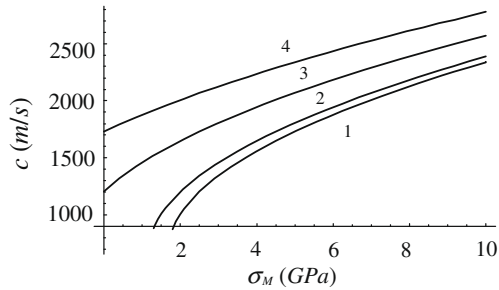
Fig. 4. Relation between interface velocity and σ_M for the 2–3–4 potential: (1) $\tau = 0$; (2) $\tau = 100$ MPa; (3) $\tau = 500$ MPa; (4) $\tau = 1000$ MPa.

For temperatures around the phase equilibrium temperature θ_e, an A region appears between martensitic variants; we study this case as well. When stresses reach and exceed the value corresponding to lattice instability, we expect that homogeneous or surface-induced nucleation occurs in addition to interface propagation, and it may interact with the interface propagation.

4.1. A–M interfaces

In Fig. 5a and b we show the evolution of two layers of M separated by A from a stationary state at $\sigma = 0$, under, respectively, tensile and compressive stresses of magnitude 500 MPa. In tension ($s_1 = 1.431$ GPa, $s_2 = -1.290$ GPa, thus metastable A and stable M) the M layers broaden by interface propagation until the A has completely disappeared, while in compression ($s_1 = 2.072$ GPa and $s_2 = 1.290$ GPa, metastable M and stable A) the M layers narrow, eventually disappearing. Note that A is unstable ($s_1 = 0$) for $\sigma = 2.733$ GPa.

In the next simulation, the initial condition is again an A–M diffuse interface in equilibrium at $\sigma = 0$. At $\sigma = 2.733$ GPa and even at $\sigma = 2.9335$ GPa, where A is unstable, the interface propagates into the A region ($s_1 < 0$, A $\rightarrow$ M), but homogeneous transformation of the unstable A does not occur. This is because $\partial G / \partial \eta = 0$ for $\eta = 0$ in our model so there is no local driving force for the transformation of A. To initiate the instability we impose the perturbation $\eta(x) = 0.01 \sin(80\pi x)$. For $\sigma = 2.5335$ GPa ($s_1 > 0$, $s_2 < 0$, A metastable) the perturbation rapidly disappears, and for $\sigma = 2.9335$ GPa ($s_1 < 0$, A unstable) the initial perturbation again disappears except near the A surface of the specimen where a M nucleus appears and grows (the nucleus energy at the surface is half that in the bulk – Levitas et al., 2003); see Fig. 6a. After complete transformation to M at the surface, the newly formed A–M interface propagates toward the first (Fig. 6a). After the interfaces meet at the point $\eta = 0$, they continue to propagate into one another until the A completely disappears. The same process occurs at the limit of A instability ($\sigma = 2.733$ GPa), but the newly formed interface moves at a lower speed.

If the initial perturbation is of the form $\eta = 0.01|\sin(40\pi x)|$ (non-symmetric with respect to $\eta = 0$) then at $\sigma = 2.5335$ GPa (A metastable), in addition to the propagating interface, the A homogeneously transforms to M. At $\sigma = 2.733$ GPa ($s_1 = 0$) and $\sigma = 2.9335$ GPa ($s_1 < 0$, A unstable) the homogeneous transformation occurs faster (Fig. 6b). If the sample is sufficiently long then the A disappears (homogeneously) before the interface reaches the surface.
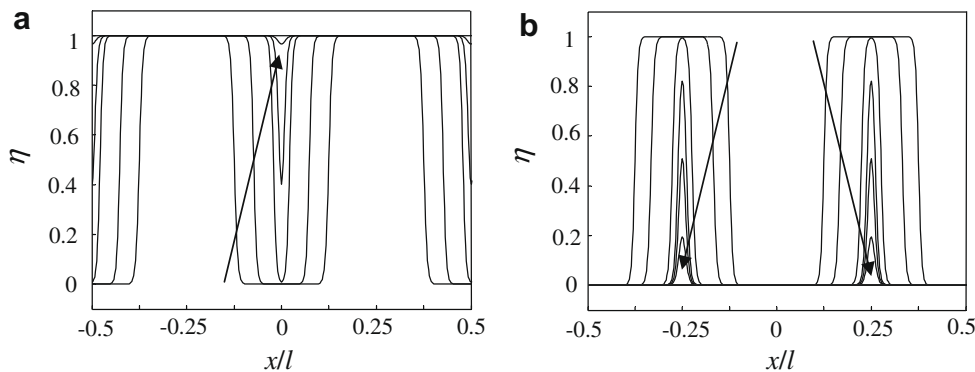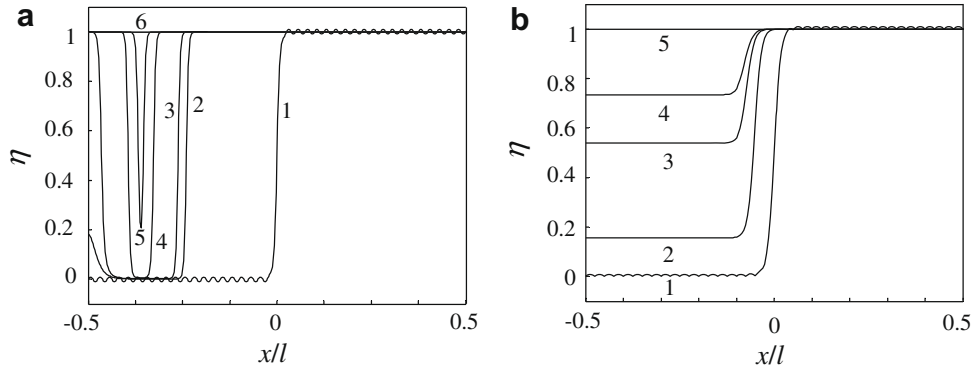

Fig. 5. Evolution of austenite–martensite microstructures. The initial condition is a stationary state of two layers of martensite at $\sigma = 0$ for $l = 27.3$ nm. (a) Under an applied stress $\sigma = 500$ MPa the layers broaden by motion of all four interfaces until the transformation is complete. (b) For $\sigma = -500$ MPa, the M layers narrow and finally disappear.

Fig. 6. Instabilities in the propagation of austenite–martensite interfaces. The initial condition is a stationary austenite–martensite microstructure at $\sigma = 0$ for $l = 27.3$ nm. (a) The perturbation $\eta(x) = 0.01 \sin(80\pi x)$ is applied. For $\sigma = 2.9335$ GPa (stress exceeding the lattice stability limit), in addition to interface propagation, a martensitic nucleus appears and grows at the sample surface. After complete transformation to M at the surface, which forms a second A–M interface, the two interfaces move toward one another until the martensitic transformation is complete. (b) Application of the perturbation $\eta(x) = 0.01 |\sin(40\pi x)|$. For $\sigma = 2.9335$ GPa (A unstable), along with interface propagation, the austenite homogeneously transforms to martensite.

4.2. $M_- — M_+$ and $M_- — A — M_+$ interfaces

In Fig. 7 we show a twinned $M_- — M_+$ microstructure, stable at $\tau = 0$. After applying the shear stress $\tau = 500$ MPa the microstructure evolves via interfaces propagation into a homogeneous M_+ final state. Note that the normal stress σ does not contribute to the driving force for $M_- — M_+$ propagation. The single interfaces propagate for any applied stress.

As A–M equilibrium ($\Delta G^\theta = 0$) is approached, an $M_- — M_+$ interface splits into $M_- — A$ and $A — M_+$ diffuse interfaces separated by a layer of A (soliton splitting – Falk, 1983; Levitas et al., 2003). In Fig. 8 we display the results of our FEM simulations of a propagating $M_- — A — M_+$ interface for $\theta = \theta_e$. We assume $\gamma = 0.2$, hence M_- loses its stability at $\tau = A/(6 - a)\gamma = 2.899$ GPa, and A loses its stability at $\tau = A/a\gamma = 2.938$ GPa, very close values. Initially, $\tau = 0$ and the interface is stationary, but under the applied shear stress $\tau = 2.689$ GPa (M_-, A metastable) the interface propagates and the width of the A layer concurrently widens (Fig. 8a). The reason for this is that the $M_- — A$ interface (metastable–metastable) propagates faster than the $A — M_+$ interface (metastable–stable); the propagating $M_- — A — M_+$ interface is stable (no A growth) if all phases are stable or metastable.

To check for an instability in the interface propagation due to A instability, an initial perturbation $\eta(x) = 0.04 |\sin 60\pi x|$ was used in the A layer. At $\tau = 2.689$ GPa (M_-, A metastable), the perturbation disappears, interface propagation is stable, and the width of the A layer increases, as in Fig. 8a. Under $\tau = 2.938$ GPa (M_- unstable, lower limit of A instability), the situation is very similar, but there are small deviations of η from zero in the A layer (Fig. 8b). For $\tau = 3.1885$ GPa (A, M_- unstable) a section of the A layer transforms to M_+ during interface propagation. This transformation runs to completion, thus forming a new stable $A — M_+$ interface that continues to propagate; shown in Fig. 8c.

The stability of the variant M_- under varying stress was studied for the initial perturbation $\eta(x) = 0.04 |\sin 60\pi x|$ in the M_- region. At $\tau = 2.689$ GPa (M_-, A metastable) the perturbation had no effect. At $\tau = 2.938$ GPa (loss of A stability) and $\tau = 3.1885$ GPa (Fig. 8d), the M_- homogeneously transforms to A as the $A — M_+$ interface propagates.
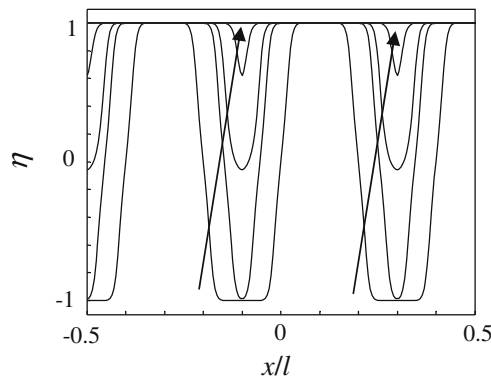
Fig. 7. The initial state is a stationary twinned martensite microstructure at $\tau = 0$, $l = 13.6$ nm. For an applied stress of $\tau = 500$ MPa, the twins disappear, resulting in a homogeneous M_+ final state.
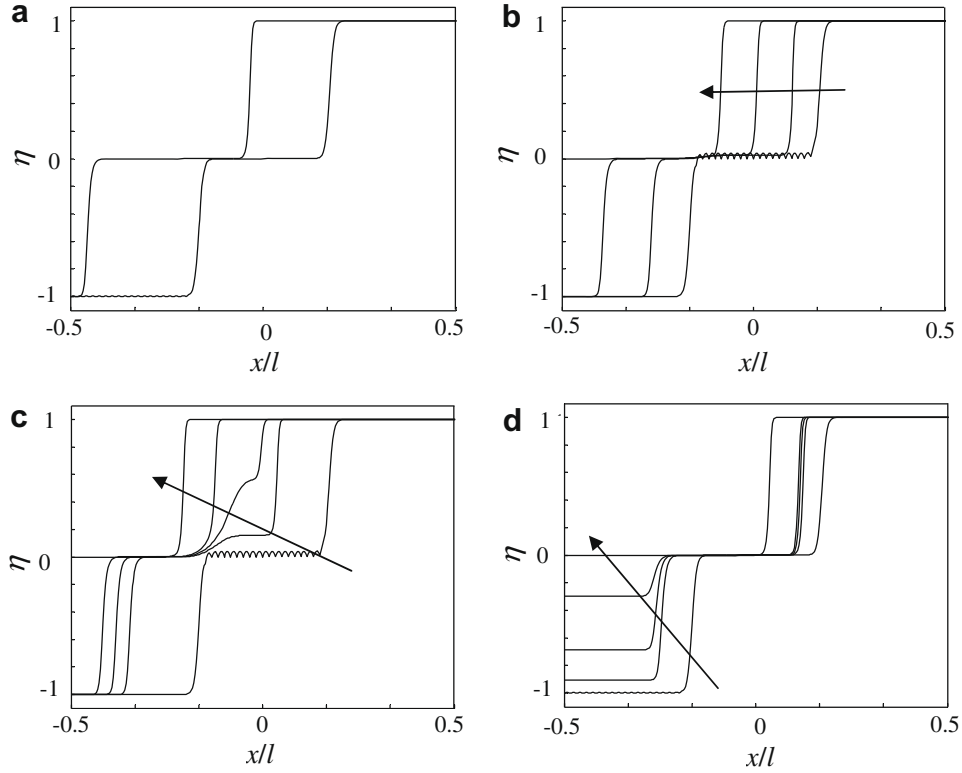
Fig. 8. Propagation of a $M_- - A - M_+$ interface and its instability; $l = 20.4$ nm. (a) For the shear stress $\tau = 2.689$ GPa (M_-, A metastable), the width of the A region widens as the interface propagates. (b) For the shear stress $\tau = 2.938$ GPa (M_- unstable, minimum stress for A instability), the initial perturbation $\eta(x) = 0.04|sin(60\pi x)|$ in the A region disappears and the interface propagation is stable. (c) For the shear stress $\tau = 3.1885$ GPa and the initial perturbation $\eta(x) = 0.04|sin\,60\pi x|$ in A, a portion of the A transforms to M_+ during interface propagation. This transformation results in a new stable $A - M_+$ propagating interface. (d) For the shear stress $\tau = 3.1885$ GPa and the initial perturbation $\eta(x) = 0.04|sin(60\pi x)|$ in the M_- region, the M_- homogeneously transforms to A as the $A - M_+$ interface propagates.

5. Three-dimensional Landau model for multivariant stress-induced martensitic phase transformations and 2D simulations

Recently (Levitas and Preston, 2002a,b; Levitas et al., 2003), a 3D Landau theory for stress-induced martensitic phase transformations was developed. It can describe phase transformations between A and M_i and between M_i variants for any crystal structures, as well as typical stress–strain curves for phase transformations in shape memory alloy, steels, and intermetallics. Also, it can incorporate all temperature-dependent thermomechanical properties of the A and M phases. The Gibbs energy G and the transformation strain tensor ε_t are of the form (Levitas and Preston, 2002a,b)

$$G = -\frac{1}{2}\boldsymbol{\sigma} : \boldsymbol{\lambda} : \boldsymbol{\sigma} - \boldsymbol{\sigma} : \boldsymbol{\varepsilon}_t - \boldsymbol{\sigma} : \boldsymbol{\varepsilon}_d + \sum_{k=1}^{n} f(\theta, \eta_k) + \sum_{i=1}^{n-1}\sum_{j=i+1}^{n} F_{ij}(\eta_i, \eta_j), \tag{42}$$

$$\boldsymbol{\varepsilon}_t = \sum_{k=1}^{n} \boldsymbol{\varepsilon}_t^k(a\eta_k^2 + (4-2a)\eta_k^3 + (a-3)\eta_k^4) - \sum_{i=1}^{n-1}\sum_{j=i+1}^{n} \eta_i^2\eta_j^2(\eta_i L_{ij} + \eta_j L_{ji}), \tag{43}$$

with

$$f(\eta_k) = A\eta_k^2 + (4\Delta G^\theta - 2A)\eta_k^3 + (A - 3\Delta G^\theta)\eta_k^4, \quad L_{ij} = (a-3)\boldsymbol{\varepsilon}_t^j + 3\boldsymbol{\varepsilon}_t^i, \quad \text{and}$$
$$F_{ij}(\eta_i, \eta_j) = \eta_i\eta_j(1 - \eta_i - \eta_j)\{B[(\eta_i - \eta_j)^2 - \eta_i - \eta_j] + D\eta_i\eta_j\} + \eta_i^2\eta_j^2(\eta_i + \eta_j)(\overline{A} - A). \tag{44}$$

Here, $\boldsymbol{\sigma}$ is the stress tensor; η_i and $\boldsymbol{\varepsilon}_t^i$ are the order parameter and the transformation strain tensor of the ith variant, where $i = 0$ corresponds to A and $\boldsymbol{\varepsilon}_t^0 = \mathbf{0}$; $\boldsymbol{\lambda}$ is the elastic compliance tensor (assumed, for simplicity, to be the same for A and M_i); and $A, \overline{A}, B$, and C are material parameters. In comparison with equations in Levitas and Preston (2002a,b) and Levitas et al. (2003), we added the eigen strain $\boldsymbol{\varepsilon}_d$ due to crystal defects (dislocation, points defects, grain and subgrain boundaries) that we will need in the next section. The parameters A and $\overline{A}$ characterize the thresholds for A $\leftrightarrow M_i$ and $M_j \leftrightarrow M_i$ transformations, while B and C control the Gibbs energy away from both the A and M_i minima and the minimum-energy paths between

the minima, therefore they do not affect the phase equilibrium and transformation conditions. The constants B and D do not contribute to phase equilibrium and instability conditions. They are used to avoid non-physical energy minima that may appear for such a complex polynomial.

The evolution of the n order parameters is described by the n coupled TDGL equations

$$\frac{\partial \eta_k}{\partial t} = -\lambda \frac{\delta G_{GL}}{\delta \eta_k} = \lambda \left(2\beta \nabla^2 \eta_k - \frac{\partial G}{\partial \eta_k} \right), \tag{45}$$

where $G_{GL} = \int_V \tilde{G}_{GL} d\Omega$ and $\tilde{G}_{GL} = G + \beta \sum_{k=1}^n (\nabla \eta_k)^2$ is the GL energy. In the following we use Eq. (16) for ΔG^θ and A, the material parameters for the cubic-tetragonal phase transformation in NiAl found in Levitas and Preston (2002a,b) and Levitas et al. (2003) and summarized in Eqs. (26) and (28), as well as

$$a = 2.980, \quad \overline{A} = 5320 \text{ MPa}, \quad B = 0, \quad D = 5500 \text{ MPa}, \quad v = 0.238, \tag{46}$$

where v is Poisson's ratio. For our 2D FEM simulations we consider just two of the three possible NiAl martensitic variants

$$\boldsymbol{\varepsilon}_t^1 = (0.215; -0.078; -0.078), \quad \boldsymbol{\varepsilon}_t^2 = (-0.078; 0.215; -0.078), \tag{47}$$

The potential (42) leads to the elasticity relation

$$\boldsymbol{\varepsilon} = \boldsymbol{\lambda} : \boldsymbol{\sigma} + \boldsymbol{\varepsilon}_t + \boldsymbol{\varepsilon}_d. \tag{48}$$

We solve Eq. (48) for the stress tensor

$$\boldsymbol{\sigma} = \boldsymbol{\lambda}^{-1} : (\boldsymbol{\varepsilon} - \boldsymbol{\varepsilon}_t) + \boldsymbol{\sigma}_d, \tag{49}$$

where we designated $\boldsymbol{\sigma}_d = -\boldsymbol{\lambda}^{-1} : \boldsymbol{\varepsilon}_d$ for an oscillatory defect stress field, which we will discuss in detail in the next Section. In addition, the standard equilibrium equations and the relationship between strains and displacements $\mathbf{u}$ are given by:

$$\nabla \cdot \boldsymbol{\sigma} = 0, \quad \boldsymbol{\varepsilon} = (\nabla \mathbf{u})_s, \tag{50}$$

where $(\cdots)_s$ means symmetrization. Thus, the complete system of equations describing the phase transformation is comprised of Eqs. (42)–(45) and (49), (50). Eqs. (43), (45), (49), and (50) are similar in structure to the coupled equations of thermoelasticity. Eq. (45) resembles a set of heat conduction equations for n temperatures η_k with temperature-dependent heat sources $\lambda \partial G / \partial \eta_k$. The transformation strain $\boldsymbol{\varepsilon}_t$ corresponds to a thermal strain with a complicated temperature dependence (43). This correspondence between phase transformation and thermoelasticity equations has important computational consequences: finite element thermoelasticity codes can be used, after some minor modifications, for phase-field model simulations of phase transformations. In contrast to approaches based on the spectral (fast Fourier transform) method (Artemev et al., 2001; Curnoe and Jacobs, 2001a,b; Jacobs et al., 2003; Jin et al., 2001; Lookman et al., 2003a,b; Rasmussen et al., 2001; Seol et al., 2003; Wang and Khachaturyan, 1997; Wang et al., 2001), the finite element approach allows us to easily expand the treatment to heterogeneous materials, large strains, arbitrary boundary conditions, and complex material models. Because the potential (42), (43) accurately describes the important features of martensitic phase transformations, we expect that our calculated microstructure evolution in this study is more realistic than that predicted by other approaches (Artemev et al., 2001; Curnoe and Jacobs, 2001a,b; Jacobs et al., 2003; Jin et al., 2001; Lookman et al., 2003a,b; Rasmussen et al., 2001; Seol et al., 2003;Shenoy et al., 1999; Wang and Khachaturyan, 1997; Wang et al., 2001). In this work we used the code FEAP (Zienkiewicz and Taylor, 2000).

We consider a square sample of size $l = 60$ nm under plane strain conditions. The temperature is $\theta = 100$ K, and at the boundaries constant stresses $\boldsymbol{\sigma}_b = (\sigma_{b1}, \sigma_{b2})$ are applied which satisfy $\mathbf{n} \cdot \nabla \eta_k = 0$, where $\mathbf{n}$ is the normal to the boundary. In our simulations, 10,000 eight-node quadrilateral finite elements were used. The thermodynamic driving force for variant–variant phase transformations due to the boundary conditions is $X_{1 \to 2}^b = \boldsymbol{\sigma}_b : (\boldsymbol{\varepsilon}_t^2 - \boldsymbol{\varepsilon}_t^1) = (\sigma_{b2} - \sigma_{b1})(\varepsilon_{t2}^2 - \varepsilon_{t1}^2) = 0.293(\sigma_{b2} - \sigma_{b1})$. The thermodynamic driving force for the $A \to M_i$ phase transformation due to boundary conditions is $X_{A \to M_i}^b = \boldsymbol{\sigma}_b : \boldsymbol{\varepsilon}_t^i = \sigma_{b1}\varepsilon_{t1}^i + \sigma_{b2}\varepsilon_{t2}^i$. Note that large internal stresses that exceed the stability limit of austenite may lead to values $\eta_i > 1$ where the Landau potential may exhibit unphysical behavior (Levitas and Preston, 2002a,b; Levitas et al., 2003). To avoid this, we enforced the constraint $\eta_i \leqslant 1$ in our numerical simulations.

In our first simulation, the initial conditions are randomly distributed η_1 and η_2 fields (Fig. 9), and the boundary conditions are $\sigma_{bi} = 10$ GPa (an arbitrary stress that provides a large driving force for the phase transformation $A \to M_i$); therefore $X_{1 \to 2}^b = 0$. The solutions of Eqs. (42)–(45) and (49), (50) are shown in Fig. 9: the first column shows the evolution of η_1, the second and third columns show the stresses σ_1 and $\sigma_1 - \sigma_2$ (since the thermodynamic driving force $X_{2 \to 1}$ is proportional to $\sigma_1 - \sigma_2$), and the last column depicts the local driving force, $\partial G / \partial \eta_1$, for the evolution of η_1. The evolution of η_2 and $\partial G / \partial \eta_2$ are qualitatively the same; for example, in the bottom figure for η_1, the dark blue field corresponds to $\eta_2 = 1$, i.e., with the variant M_2. After passing through a complex microstructure containing plates, laths, and needles the solution converges to a primitive $M_1 - M_2$ twin microstructure (Fig. 9). Stresses and local driving forces are concentrated at the interfaces, and local driving forces are quite low. However, this microstructure is not stable – driven by a decrease in gradient energy through a reduction in interface area it converges to a single phase, M_1 or M_2, depending upon initial conditions. The propagation direction of each planar interface as well as the final state variant can be easily predicted: each interface moves to reduce its length, thus the variant occupying the central part of the sample is the survivor.
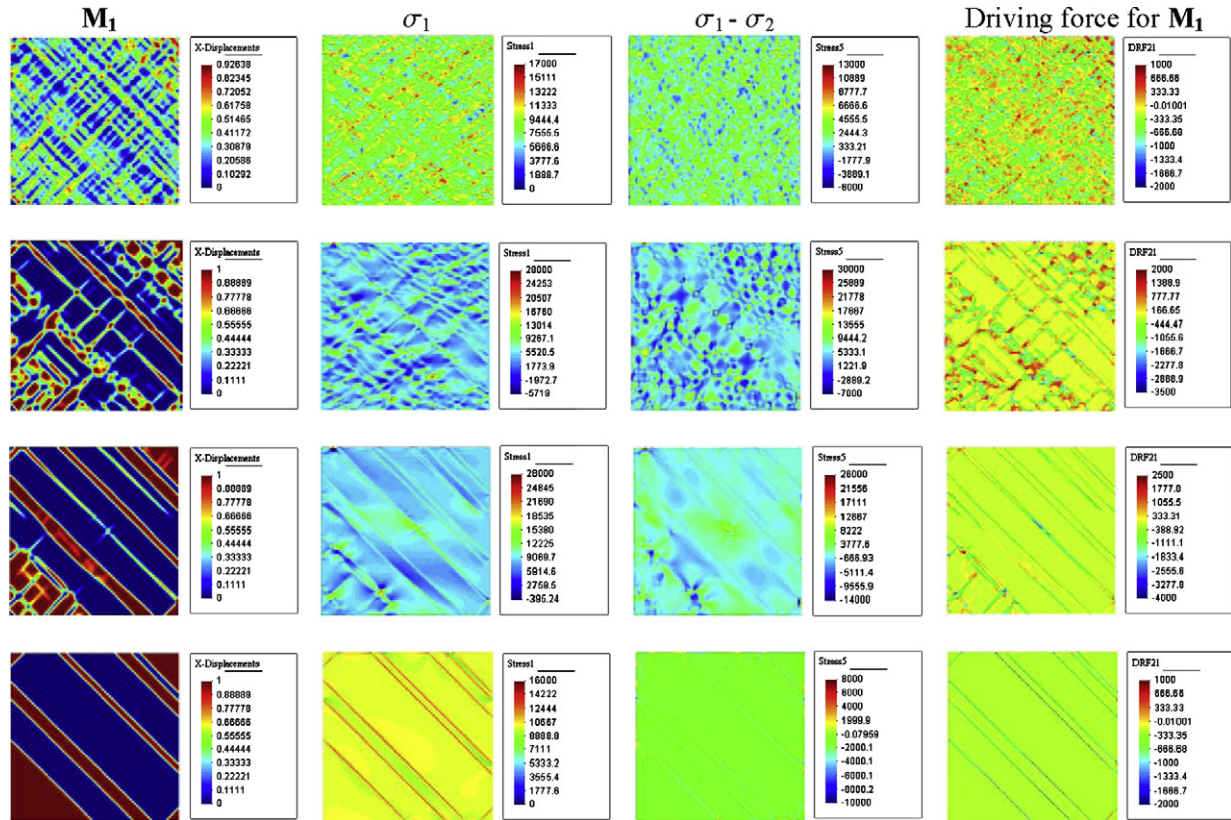
Fig. 9. Evolution of initially randomly distributed fields η_1 and η_2 (first column), σ_1 and $\sigma_1 - \sigma_2$ (second and third columns), and the local driving force, $\partial G/\partial \eta_1$, for evolution of η_1 (right column) for $\sigma_{b1} = \sigma_{b2} = 10$ GPa. The microstructure finally converges to homogeneous M$_2$ with zero internal stresses and driving forces.

Note that the normals to the interfaces vary from parallel to the boundary in a very thin surface layer (due to the boundary condition $\mathbf{n} \cdot \nabla \eta_k = 0$) to 45° to the boundaries (determined by elastic energy minimization). This is typical of all simulations below but difficult to see in the figures.

In our second simulation, the initial conditions are $\eta_1 = \eta_2 = 0.1$ in a circle of radius 2 nm (an embryo) at the center of the sample and zero elsewhere. The boundary stresses are $\sigma_{b1} = \sigma_{b2} = 15$ GPa; hence, the system is initially symmetric with respect to each variant. A very complicated microstructure consisting of a combination of four herring bone types of microstructure is developed (Fig. 10). At some stage, the equivalence of both variants is violated-units of M$_2$ coalesce at the center, and M$_1$ coalesces in four triangles near the sample boundaries. Other units evolve to a needle-like microstructure (similar to that observed experimentally in Abeyaratne et al. (1996)). Later, the solution evolves into a primitive twinned microstructure and finally to homogeneous M$_2$.

Thus, as discussed in the Introduction, in both of these simulations, for which the boundary stresses are specified, the lack of athermal friction leads asymptotically to a single phase.

6. Athermal threshold for interface propagation

The above equations are valid when the magnitude of the driving force exceeds all barriers due to point and line defects, as well as the Peierls barrier, because these barriers were not included in the preceding analysis. At these high driving forces the interface motion is governed by the phonon (and at lower temperatures, by the electron) drag mechanism, but the barriers, which result in an athermal friction force opposing the interface motion (Ghosh and Olson, 1994; Grujicic et al., 1985; Olson and Cohen, 1986), must be taken into account at lower driving forces. As discussed in the Introduction, the inclusion of an athermal threshold in the phase field approach is not straightforward because the phase field approach does not involve a separate equation for the interface but rather an evolution equation for the order parameter. We can put, for example, $\lambda = 0$ if $|s_2/12| < K$, however, this can arrest unphysical intermediate configurations, thus the system never converges to a realistic microstructure consisting of A and M variants separated by diffuse interfaces, either stationary or moving. We now propose two schemes for solving this problem.
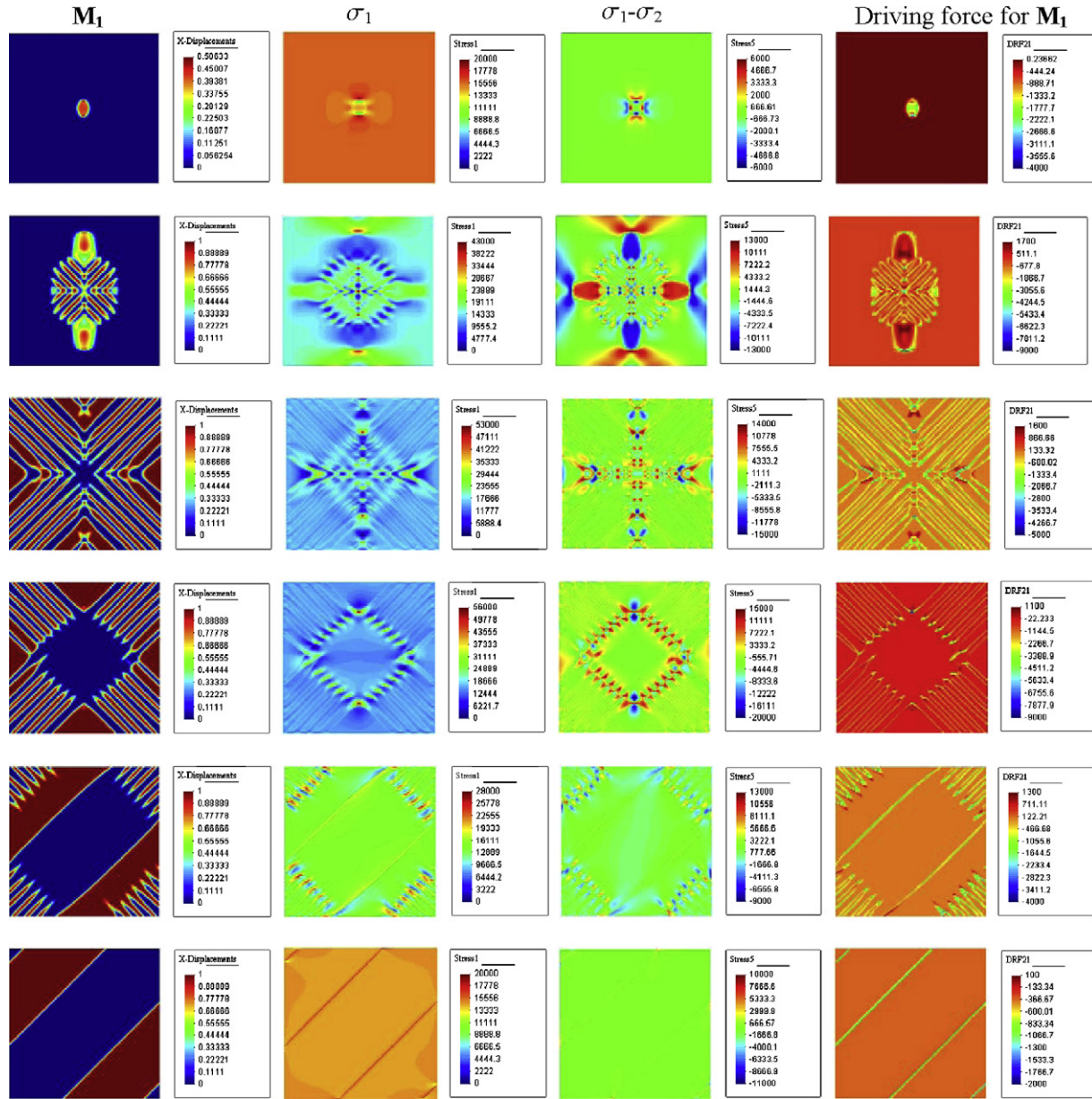
Fig. 10. Evolution of an embryo, $\eta_i = 0.1$, in a circle of radius of 2 nm at the center of the sample for $\sigma_{bi} = 15$ GPa. Left column: η_1; second and third columns: σ_1 and $\sigma_1 - \sigma_2$; right column: $\partial G/\partial \eta_1$, the local driving force for evolution of η_1. The stationary microstructure is M_2. In the first two rows, red is M_1, and the blue outside of the M_1 regions is A; the distribution for M_2 is rotated 90° from the distribution for M_1. In the last four rows, red is M_1 and blue is M_2. (For interpretation of the references to color in this figure legend, the reader is referred to the web version of this paper.)

6.1. Athermal threshold I: modified evolution equations

To introduce a threshold for interface propagation, we need to find a way to distinguish between interface propagation and an arbitrary non-stationary process. At all points of the propagating interface $(\partial \eta/\partial t)/(\partial \eta/\partial x) = \pm c$; therefore, the spatial derivative of this expression is zero, which results in

$$R := \frac{\partial^2 \eta}{\partial x \partial t} \frac{\partial \eta}{\partial x} - \frac{\partial \eta}{\partial t} \frac{\partial^2 \eta}{\partial x^2} = 0. \tag{51}$$

Near the interface, $|R| \ll 1$. We can account for interface friction by requiring very slow dynamics, which is realized for very small values of the kinetic coefficient λ, in narrow bands around the interfaces if the driving force is less than a critical value, K:

$$\lambda = o \quad \text{for } |R| < \varsigma \text{ and } |s_2/12| < K, \qquad \lambda = \lambda_0 \quad \text{otherwise.} \tag{52}$$

Here ς is a small quantity of order the computational error, and o is sufficiently small that $\partial\eta/\partial t$ is negligible. We use o instead of zero to avoid $\lambda = 0$ at points where $\partial\eta/\partial t = \partial\eta/\partial x = 0$ ($R = 0$), but which do not belong to the moving interface, e.g., at the maximum of a critical M nucleus.

Fig. 11 shows the results of a numerical simulation of the evolution of an initial sinusoidal order parameter (2–4–6 potential, $\Delta G^\theta = 0$). First, two $M_-(\eta = -1)-M_+(\eta = 1)$ interfaces are formed but their motion is arrested because $|s_2/12| < K$. The magnitude of the driving force is then increased above the threshold K (by increasing τ) and the interfaces begin moving toward each other. They first meet at the point $(x,\eta) = (0,-1)$. Subsequently, $\eta(0,t)$ increases toward $\eta = +1$ until M_- completely disappears, resulting in a final state of homogeneous M_+. It is clear that our goal has been accomplished: interface motion can be both arrested and released, while intermediate unstable configurations are not affected by the athermal threshold.

Eq. (52) has the drawback that the kinetic coefficient λ and the interface velocity jump from zero to a finite value at $|s_2/12| = K$. However, experimental observations (Ghosh and Olson, 1994; Grujicic et al., 1985; Levitas et al., 2002c; Olson and Cohen, 1986) show, and sharp interface theory predicts, that the magnitude of the interface velocity depends on the excess of the driving force over the athermal threshold, $s_2/12 - K$ for $s_2/12 > K$ and $s_2/12 + K$ for $s_2/12 < -K$, rather than on $|s_2/12|$. Note that these replacements are equivalent to $\boldsymbol{\sigma} : \boldsymbol{\varepsilon}_t \to \boldsymbol{\sigma} : \boldsymbol{\varepsilon}_t \pm K$. If the athermal threshold is caused by the stress fields of various crystal defects, then all occurrences of $\boldsymbol{\sigma} : \boldsymbol{\varepsilon}_t$ in Eqs. (13) and (14) for c_4 and c_6 must be replaced by $\boldsymbol{\sigma} : \boldsymbol{\varepsilon}_t \pm K$. Thus, the interface speeds for $|s_2/12| \geqslant K$ are

$$c_4 = \lambda_4 \sqrt{\beta} \frac{s_2(1 - K/|s_2/12|)}{\sqrt{4s_1 - s_2 + sign(s_2)4(3-a)K}} \tag{53}$$

$$c_6 = \lambda_6 \sqrt{\frac{2\beta}{3}} \frac{s_2(1 - K/|s_2/12|)}{\sqrt{3s_1 - s_2 + sign(s_2)3(4-a)K}} \tag{54}$$

The interface speeds Eqs. (53) and (54) can be incorporated in our phase field model through λ_0 (kinetic coefficient for $|s_2/12| \geqslant K$; see Eq. (52)) defined by requiring that c_4 and c_6 as given by Eqs. (13) and (14) with $\lambda \to \lambda_0$ are equal to the corresponding velocities in Eqs. (53) and (54):

$$\lambda_{04} = \lambda_4 \frac{1 - K/|s_2/12|}{\sqrt{1 + 4\,sign(s_2)(3-a)K/(4s_1 - s_2)}} \tag{55}$$

$$\lambda_{06} = \lambda_6 \frac{1 - K/|s_2/12|}{\sqrt{1 + 3\,sign(s_2)(4-a)K/(3s_1 - s_2)}} \tag{56}$$

For the general case of three dimensions and multivariant phase transformations described by m order parameters η_i, $(\partial\eta_i/\partial t)/|\nabla\eta_i| = \pm c$ on the interface. The local direction of interface propagation is $\mathbf{n} := \nabla\eta_i/|\nabla\eta_i|$; let r be the local coordinate along $\mathbf{n}$. Then $(\partial\eta_i/\partial t)/(\partial\eta_i\partial r) = \pm c$ at all points of the interface. Again setting the r derivative to zero yields

$$R_i := \frac{\partial^2\eta_i}{\partial r\partial t}\frac{\partial\eta_i}{\partial r} - \frac{\partial\eta_i}{\partial t}\frac{\partial^2\eta_i}{\partial r^2} = 0. \tag{57}$$

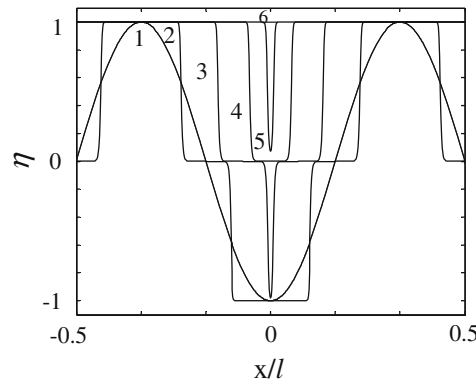For each i we can express λ_i in the same way as in Eq. (52).

Fig. 11. Numerical simulation of the evolution of the initial configuration (curve 1) $\eta(x) = cos(\pi x/2)$ for the threshold-type kinetics defined by Eq. (52). The initial configuration evolves into two M_--M_+ interfaces (curve 2) which are arrested due to the condition $|s_2/12| < K$. Subsequently, $|s_2/12|$ is increased above the threshold K and interfaces move toward each other. They first meet at the point $(x,\eta) = (0,-1)$ and then $\eta(0,t)$ increases toward $\eta = +1$ leading to complete disappearance of M_- and to a homogeneous M_+ structure.

Our approach can also be used for thermally activated interface motion, which is described, for example, by the equation (Ghosh and Olson, 1994; Grujicic et al., 1985)

$$c = c_s \, exp\left[-\frac{Q_0}{k\theta}\left(1 - [(|s_2/12| - K)/W_0]^p\right)^b\right], \tag{58}$$

where Q_0 is the activation energy, W_0 is the height of the driving force barrier corresponding to the rate-controlling (short-range) obstacles, k is the Boltzmann constant, and p and b are constants. All of the material parameters appearing in (58) have been estimated for Fe–22.31Ni–2.888Mn alloy (Table 1 in Levitas et al., 2002c). As above, we can define threshold-dependent kinetic coefficients λ_{04} and λ_{06} by equating c_4 and c_6 as given by Eqs. (13) and (14) with $\lambda \to \lambda_0$ to c from Eq. (58).

Note that for $\Delta G^\theta - \sigma\varepsilon = 0$, the limit condition for the A $\to$ M$_+$ transformation, $X_{A\to M_+} = -s_2/12 = \tau\gamma = K$, and that for the M$_-$ $\to$ A transformation, $X_{M_-\to A} = s_2/12 = \tau\gamma = K$, result in $X_{M_-\to M_+} = X_{A\to M_+} + X_{M_-\to A} = 2\tau\gamma = 2K$, i.e., the threshold for M$_-$ $\to$ M$_+$ interface propagation is $2K$. In this case a finite A region appears between the martensitic variants, and there is no need to introduce a separate threshold condition for variant–variant transformations. We consider only the case where the interface moves into M$_-$; the opposite case leads to identical conditions for interface propagation. If $\Delta G^\theta - \sigma\varepsilon \neq 0$, then $X_{A\to M_+} \neq X_{M_-\to A}$ and it is possible that, for example, $X_{M_-\to A} < 0$, in which case the transformation condition $X_{M_-\to A} \geqslant K$ for the $M_- - A$ interface cannot be satisfied. This means that one must consider the M$_-$ $\to$ M$_+$ interface separately and apply the condition

$$\lambda = o \quad \text{for } |R| < \varsigma \text{ and } |\tau\gamma| < K, \qquad \lambda = \lambda_0 \quad \text{otherwise}. \tag{59}$$

6.2. Athermal threshold II: oscillatory defect stress fields

Usually, kinetic equations for thermally activated dislocation (Kocks et al., 1975) or interface motion are derived by considering spatially oscillatory energy profiles that represent the Peierls barrier or the energy profiles of various defects (Ghosh and Olson, 1994). We will introduce a spatially oscillatory energy profile through oscillatory stress fields, σ_d, due to defects; the stress tensor is given by Eq. (49). If, for example, $\sigma_d = K\varepsilon_{t1} sin(2\pi x/b)/(\varepsilon_{t1} : \varepsilon_{t1})$, then the Landau potential contains an additional transformation work, $K\,sin(2\pi x/b)$, which produces an effect similar to an interface friction K for motion in both directions. A similar effect can be obtained by adding $K\,sin(2\pi x/b)$ to the change in the thermal part of the Gibbs energy, ΔG^θ.

The period b is determined by the actual field of defects. If the origin of the athermal threshold is the Peierls barrier, then b is the period of the crystal lattice. If the stress field is due to stochastically distributed dislocations, then the period is the averaged distance between dislocations, a well-known length scale. Multiple length scales would be present in a more detailed treatment of the system of dislocations.
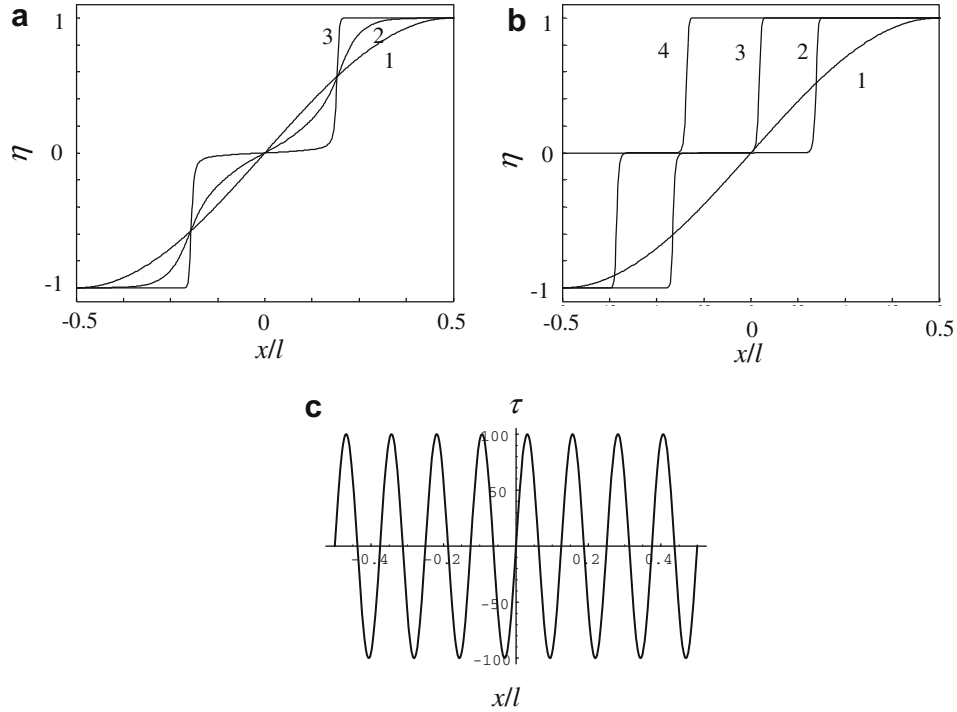
The evolution of an initial sinusoidal $\eta(x)$ (2–4–6 potential) under the shear stress $\tau = 75$ MPa is shown in Fig. 12. In the absence of the periodic field, the solution evolves to M$_+$, but in contrast, a M$_-$–A–M$_+$ microstructure (Fig. 12a, configuration 3) is formed in the presence of the periodic stress field $\tau_d = -100\,sin(8\pi x)$ MPa (Fig. 12c). After increasing the stress τ to 125 MPa, the M$_-$–A–M$_+$ interface propagates to the left (Fig. 12b).

7. Microstructure evolution in the presence of oscillatory defect stress fields

In all calculations we use the material parameters for the cubic–tetragonal transformation in NiAl. We perform 2D simulations, impose the boundary stress $\sigma_{b1} = \sigma_{b2} = 10$ GPa, take $\theta = 100$ K, and consider only the two NiAl martensitic variants with transformation strains $\varepsilon_t^1 = (0.215; -0.078; -0.078)$ and $\varepsilon_t^2 = (-0.078; 0.215; -0.078)$. For $\sigma_d = (\sigma_{d1}, \sigma_{d2})$, the thermodynamic driving force for the M$_1$ $\to$ M$_2$ phase transformation due to the defect stress fields is $X_{1\to 2}^d = \sigma_d : (\varepsilon_t^2 - \varepsilon_t^1) = \Delta\varepsilon_t(\sigma_{d2} - \sigma_{d1})$, where $\Delta\varepsilon_t = \varepsilon_{t2}^2 - \varepsilon_{t2}^1 = \varepsilon_{t1}^1 - \varepsilon_{t1}^2 = 0.293$. The thermodynamic driving force for the A $\to$ M$_i$ phase transformations due to the stress fields of the defects is $X_{A\to M_i}^d = \sigma_d : \varepsilon_t^i = \sigma_{d1}\varepsilon_{t1}^i + \sigma_{d2}\varepsilon_{t2}^i$. In the particular case $\sigma_{d2} = \sigma_{d1}$ one has $X_{1\to 2}^d = 0$ and $X_{A\to M_i}^d = \sigma_{d1}(\varepsilon_{t1}^i + \varepsilon_{t2}^i)$.

We study four classes of problems. Some preliminary results can be found in Levitas and Lee (2007).

1. Solution to the same problem as in Fig. 9 (random initial distribution of A and M) but with the periodic defect stress field $\sigma_{d2} = -\sigma_{d1} = 10\,sin(16\pi x)\,sin(16\pi y)$ and consequently $X_{1\to 2}^d = 20\Delta\varepsilon_t\,sin(16\pi x)\,sin(16\pi y)$; see Fig. 13. In the absence of surface energy and internal stresses due to transformation strain, a minimum of the energy would correspond to multi-connected microstructures with M$_1$ (M$_2$) in the regions with $X_{1\to 2}^d < 0$ ($X_{1\to 2}^d > 0$). This is essentially the case in the first row of Fig. 13. The elastic energy due to evolving transformation strain fields (within evolving martensitic regions) promotes the appearance of straight plates aligned at 45°, and surface energy reduction drives coalescence. In this stage, elastic and surface energy exceed the potential barriers due to the $X_{1\to 2}^d$ field, and the units coalesce in two orthogonal groups of twinned plates. One group eventually predominates, resulting in a stationary microstructure comprised of equidistant twinned plates. Our periodic fields do not arrest any intermediate microstructures ($0 < \eta_i < 1$), nor do they change the orientation of the martensitic plates which is determined by minimization of elastic energy, but they do slightly distort the otherwise planar interfaces.

Fig. 12. Evolution of an initial sinusoidal $\eta(x)$ (curve 1) in the periodic defect stress field $\tau_d(x) = -100\sin(8\pi x)$ MPa shown in (c). (a) Under a shear stress $\tau = 75$ MPa, a $M_- - A - M_+$ split interface is formed (curve 3). (b) After increasing the shear stress to 125 MPa, the $M_- - A - M_+$ interface propagates to the left.

Fig. 14 shows the solution to the same problem as in Fig. 8 but with equal periodic stress fields of defects $\sigma_{d2} = \sigma_{d1} = 10\sin(16\pi x)\sin(16\pi y)$ (and consequently $X_{1\to s2}^d = 0$). Again, elastic energy due to evolving transformation strain fields (within evolving martensitic regions) promotes the appearance of straight plates aligned at 45°, and the surface energy promotes coalescence.

The field $X_{M_i\to A}^d$ affects the initial stages of formation of the microstructure, reducing the initial M_i units to sizes comparable to its period. In this stage, the elastic and surface energies exceed the potential barriers due to the $X_{M_i\to A}^d$ field, and the units coalesce. Once the system has converged to a twin microstructure topologically similar to that in Fig. 9, it is arrested because the elastic and surface energies cannot overcome the barriers due to the $X_{M_i\to A}^d$ field. The widths of different martensitic plates vary by several times, and for most plates the width exceeds the half period of the field $X_{M_i\to A}^d$. Consequently, small islands of incompletely transformed A, stabilized by the $X_{M_i\to A}^d$, appear within broad martensitic plates, as can be seen in Fig. 14. If the boundary stresses σ_{bi}, and consequently $X_{A\to M_i}^b$, are decreased, then these islands will serve as heterogeneous nucleation sites for A. Although the volume fractions of M_1 and M_2 vary with the initial conditions, the volume fraction of M_1 is invariably larger than that of M_2. The presence of both M_1 and M_2 is due entirely to the defect stress field-if removed, the final microstructure consists of M_1 or M_2 only, depending on initial conditions. Even though $X_{1\to2}^d = 0$, the stress field of the defects nevertheless forms a mixed $M_1 - M_2$ microstructure because it arrests the formation and propagation of $A - M_i$ interfaces.

2. For the fields $\sigma_{d1} = 5\cos(16\pi x)\cos(16\pi y)$ and $\sigma_{d2} = 5\sin(16\pi x)\sin(16\pi y)$, $X_{1\to2}^d = -5\Delta\varepsilon_t\cos(16\pi(x+y))$, which is periodic along the diagonal. The initial microstructure evolves into a perfect, alternating, equally sized $M_1 - M_2$ microstructure oriented at 45° (Fig. 15). The widths of the M_i plates are determined by the period of the oscillating stress field-there is no lateral coalescence of M_i plates.

Next – see Fig. 16 – the stationary microstructure obtained in the previous simulation (Fig. 14) was taken as an initial condition, with $\sigma_{bi} = 10$ GPa. The defect stress field is removed ($X_{1\to2}^d = 0$), thus there is no athermal threshold or hysteresis. After removal of σ_{di} the M_1 plates widen at the expense of M_2 until the transformation to M_1, driven by the reduction of surface energy, is complete.

When, prior to phase transformation completion, the stress σ_{b1} at the boundary was decreased to 9.9 GPa, the reverse phase transformation $M_1 \to M_2$ occurred by equal widening of all M_2 plates until the transformation was complete.

In Fig. 17 we plot interface velocity v vs. the macroscopic driving force $X_{1\to2}^b$ for four interfaces from the microstructure in Fig. 16. The small, non-zero velocity for $X_{1\to2}^b = 0$ is caused by the driving force due to the reduction of surface energy; with increasing $X_{1\to2}^b$, the contribution of the surface energy is negligible. All of these points can be approximated by $v = -0.005 + 0.0034X_{1\to2}^b$ with very small v for $X_{1\to2}^b = 0$. For an interface of constant length, $v = 0$ for $X_{1\to2}^b = 0$, which is also confirmed by our 1D analytical solution. Thus, the athermal threshold and hysteresis are absent.
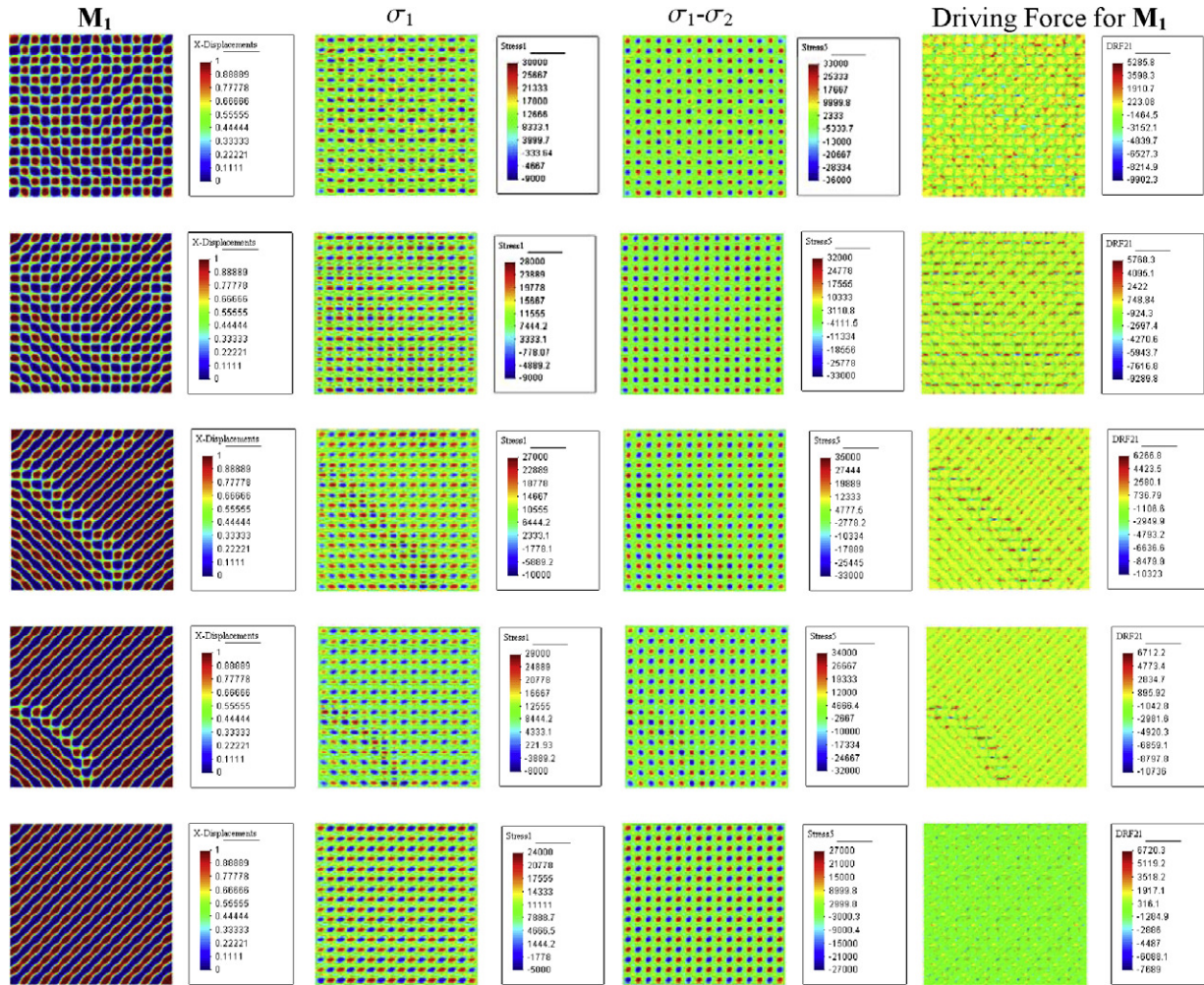
Fig. 13. Solution to the same problem as in Fig. 9 but with the periodic defect stress field $\sigma_{d2} = -\sigma_{d1} = 10\sin(16\pi x)\sin(16\pi y)$. Left column: η_1; second and third columns: σ_1 and $\sigma_1 - \sigma_2$; right column: the local driving force, $\partial G/\partial\eta_1$, for the evolution of η_1. The bottom row is the stationary solution (red is M_1 and blue is M_2). (For interpretation of the references to color in this figure legend, the reader is referred to the web version of this paper.)

For the same initial and boundary conditions, the defect stress field $\sigma_{d1} = \sigma_{d2} = 10\sin(8\pi(x+y))$ leads to $X_{1\to2}^d = 0$ and to $X_{A\to M_i}^d$ a periodic function along the diagonal. The initial microstructures coalesce into alternating M_1-M_2 plates of different widths oriented at 45°; Fig. 18.

3. In Fig. 19 we simulate the evolution of a stochastic initial distribution of M_1 and M_2 in a defect stress field for which $\sigma_{d2} - \sigma_{d1}$ is a 2D plane square wave (in general, the periodic extension of the function $C[\theta(r) - \theta(-r)]$ on $-b \leqslant r \leqslant b$, where C is a constant, r is the coordinate along the normal to the wave, and $2b$ is the wavelength). We superimpose equal period, in-phase square waves for σ_{d2} and $-\sigma_{d1}$, each with an amplitude of 2 GPa, a wavelength of $0.2l$, and normals inclined 45° (Fig. 19). The amplitude of the $\sigma_{d2} - \sigma_{d1}$ square wave is 4 GPa ($|X_{1\to2}^d| = \Delta\varepsilon_t|\sigma_{d2} - \sigma_{d1}| = 4\Delta\varepsilon_t$ GPa = 1.172 GPa), thus the expected stress hysteresis is $H = |\sigma_{d2} - \sigma_{d1}| = 4$ GPa. Indeed, keeping $\sigma_{b2} = 10$ GPa for $6 < \sigma_{b1} < 14$ GPa the interfaces do not move; for $\sigma_{bi} = 10$ GPa the system converges to a twinned microstructure with twins occupying the regions of positive and negative $X_{1\to2}^d$. Only for $\sigma_{b1} > 14$ GPa ($\sigma_{b1} < 6$ GPa) does the variant M_1 (M_2) grow until the phase transformation is complete. Thus plane square wave defect stress fields produce a finite, rate-independent athermal hysteresis (deviation from $X_{1\to2}^b = 0$ (equilibrium) needed to initiate interface motion). Note that the local driving force $\partial G/\partial\eta_i$ is concentrated at the interfaces because it is zero for both $\eta_i = 0$ and $\eta_i = 1$; internal stresses are also concentrated at the interfaces.

The evolution of stochastic initial data under $\sigma_{b1} = \sigma_{b2} = 10$ GPa in the presence of the equal square wave defect stress fields $\sigma_{d2} = \sigma_{d1} = \pm 10$ GPa (i.e., $X_{1\to2}^d = 0$) with $b = 0.2l$ and inclined at 45° is shown in Fig. 20. The stationary solution (last row) consists of M_i plates in the regions of positive stress separated by A plates in the regions of negative stress.

Instead of a plane square wave, one can smooth the transition from $-H$ to H with a continuous function defined in a band of width b_t. In this case, a change in stress $\sigma_{b2} - \sigma_{b1} \sim X_{1\to2}^d$ below the threshold value will induce only a slight movement of the interfaces that depends on the stress field within b_t. If $b_t \ll b$, this interface motion does not significantly change the
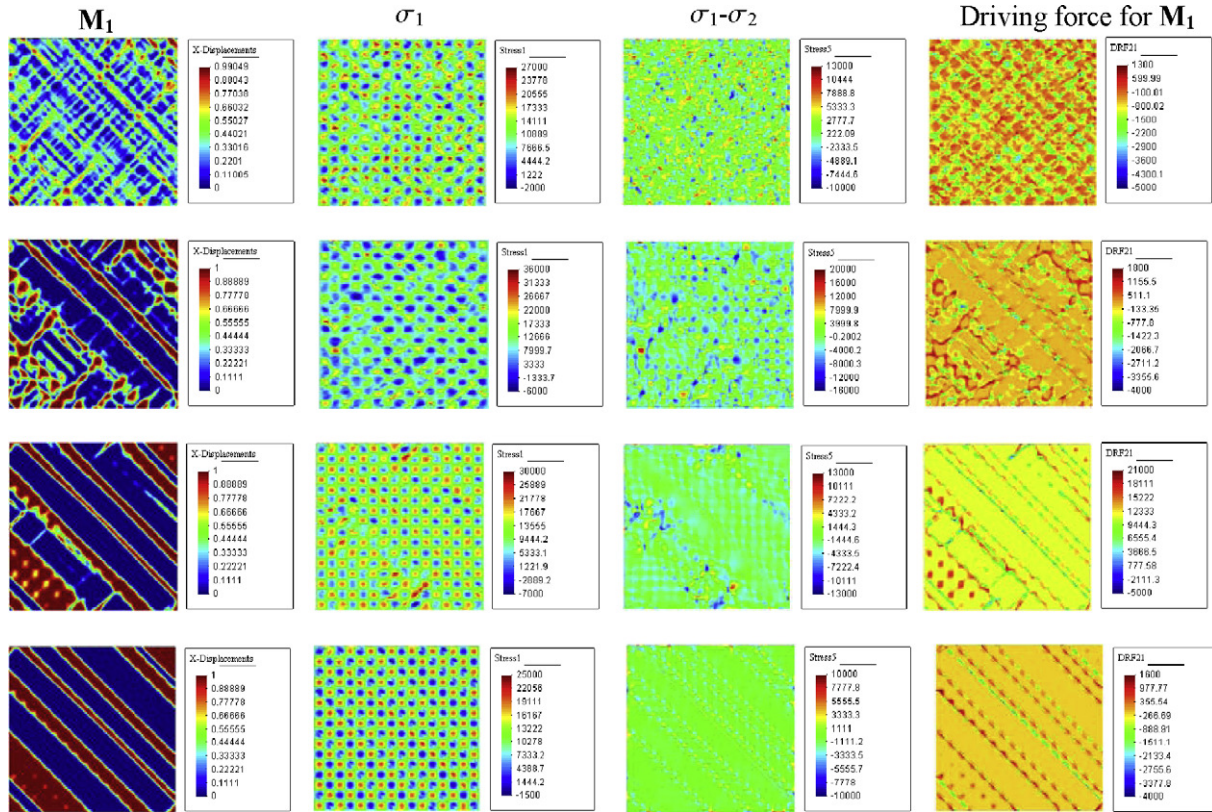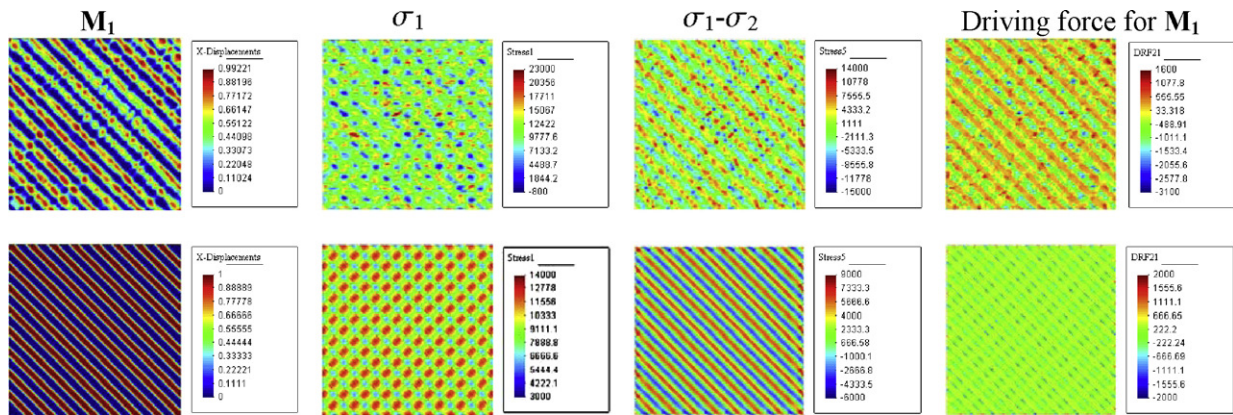
Fig. 14. Solution to the same problem as in Fig. 9 but with the periodic stress field $\sigma_{d1} = \sigma_{d2} = 10\sin(16\pi x)\sin(16\pi y)(X_{1\to2}^d = 0)$. Left column: η_1; second and third columns: σ_1 and $\sigma_1 - \sigma_2$; right column: the local driving force, $\partial G/\partial\eta_1$, for evolution of η_1. The bottom row is the stationary solution in which red is M_1 and blue is M_2. The small islands within broad M_1 plates are incompletely transformed A stabilized by the field $X_{A\to M_1}^b$ of defects. If $X_{A\to M_1}^b$ is reduced then these islands will serve as heterogeneous nucleation sites for A. (For interpretation of the references to color in this figure legend, the reader is referred to the web version of this paper.)

Fig. 15. Solution to the same problem as in Fig. 9 but with the periodic defect stress field $\sigma_{d1} = 5\cos(16\pi x)\cos(16\pi y)$ and $\sigma_{d2} = 5\sin(16\pi x)\sin(16\pi y)$ for which $X_{1\to2}^d = -5\Delta\varepsilon_t\cos(16\pi(x+y))$, a periodic function along the diagonal. Left column: η_1; second and third columns: σ_1 and $\sigma_1 - \sigma_2$; right column: the local driving force, $\partial G/\partial\eta_1$, for evolution of η_1. The bottom row is the stationary solution (red is M_1 and blue is M_2). (For interpretation of the references to color in this figure legend, the reader is referred to the web version of this paper.)

volume fraction of twins. But if $b_t \simeq b$, a variation in stress below the threshold value changes the stationary microstructure and twin concentration continuously and significantly. In particular, for $\sigma_{d1} = 5\cos(6\pi x)\cos(6\pi y)$ and $\sigma_{d2} = 5\sin(6\pi x)\sin(6\pi y)$ $(X_{1\to2}^d = -5\Delta\varepsilon_t\cos(6\pi(x+y)))$ $(H = 5\,\text{GPa})$ and $\sigma_{bi} = 10\,\text{GPa}$, we obtained the same stationary structure as for the square wave fields. However, when we varied σ_{b1} between 5 and 15 GPa, the concentration and widths of all stationary twins
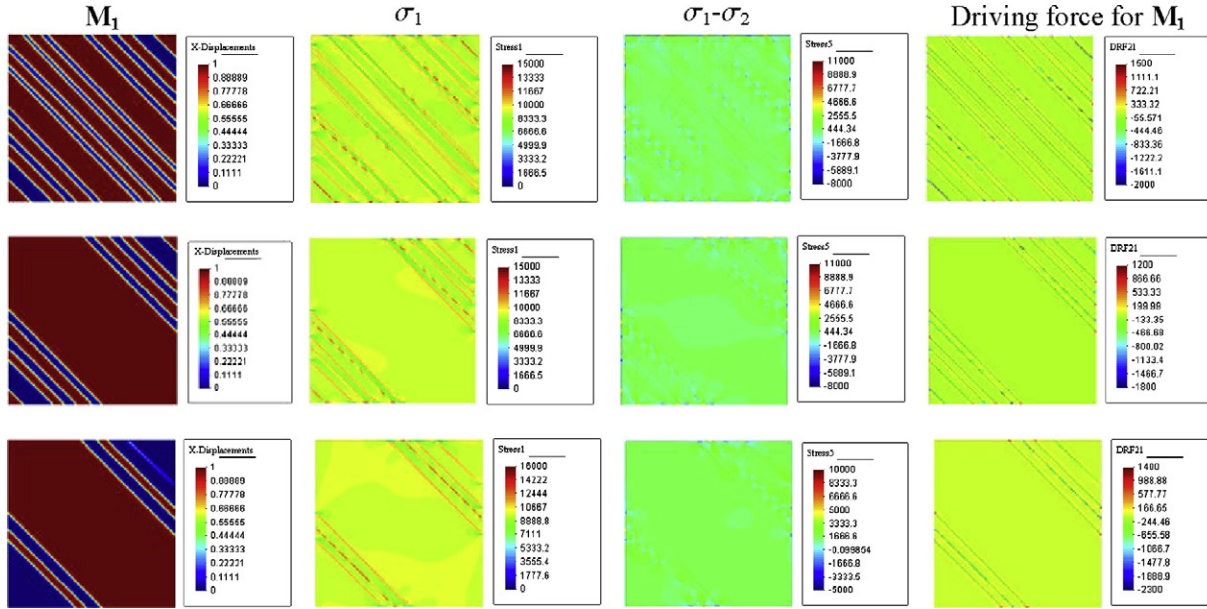
Fig. 16. Evolution of the initially stationary microstructure obtained in the previous simulation (Fig. 14) after removal of the defect stress field σ_{di}. At first, for $\sigma_{bi} = 10$ GPa, the M_1 plates widen, but then, before the transformation is complete, the boundary stress σ_{b1} is decreased to 9.9 GPa. Variant M_2 grows by coalescence of the plates, finally converging to homogeneous M_2 with zero internal stresses and driving forces. Left column: η_1; second and third columns: σ_1 and $\sigma_1 - \sigma_2$; right column: the local driving force for evolution of η_1, $\partial G/\partial \eta_1$. The red corresponds to M_1 and blue to M_2. (For interpretation of the references to color in this figure legend, the reader is referred to the web version of this paper.)
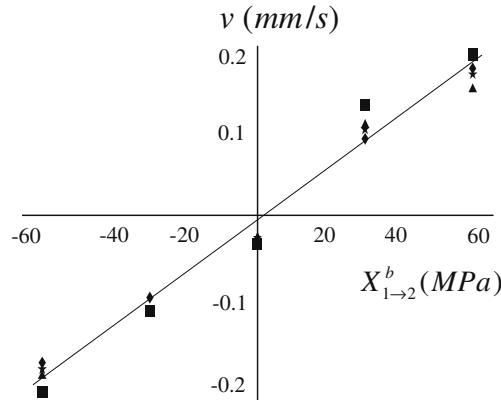

Fig. 17. Interface velocity v vs. the macroscopic driving force $X_{1\to2}^b$ for four interfaces from the microstructure in Fig. 16.

varied continuously and coalesced to pure M_2 (or M_1) at 5 GPa (or 15 GPa) (Fig. 21). We emphasize that the slow cyclic stress–twin concentration curve *does not exhibit a hysteresis loop and energy dissipation.*

4. In Fig. 22 we display the evolution of an embryo with $\eta_i = 0.1$ as in Fig. 10 but with the addition of the periodic defect fields $\sigma_{d1} = 5\cos(16\pi x)\cos(16\pi y)$ and $\sigma_{d2} = 5\sin(16\pi x)\sin(16\pi y)$. The defect fields completely change the microstructure evolution. The stationary solution is a twinned structure with equal width twins, where M_2 (or M_1) is located in regions with positive (or negative) values of $X_{1\to2}^d = -5\Delta\varepsilon_t\cos(16\pi(x+y))$. Around two opposite corners M_1 units evolve into triangles.

For the same problem but with equal defect stresses $\sigma_{d1} = \sigma_{d2} = 10\sin(16\pi(x))\sin(16\pi y)$ ($X_{1\to2}^d = 0$), the symmetry of the problem is changed from the very beginning, and $X_{A\to M_i}^d$ drives the microstructure to four twinned regions, as seen in Fig. 23. One can also see multiple nucleation of new M_2 (and M_1) units around the maxima of $X_{A\to M_i}^d$. Thus, the stress fields of the defects not only produce an athermal threshold but also create sites for heterogeneous nucleation. However, the driving force due to decreases in the energy associated with internal stresses and the surface energy exceeds the barriers due to $X_{A\to M_i}^d$. Coalescence of M_1 occurs and the final stationary solution is a two-twin microstructure.

Results for the same problem but with the magnitude of the oscillatory field increased to 20 GPa are shown in Fig. 24. The stationary microstructure consists of four twins with islands of incompletely transformed material, which may serve as nucleation sites for austenite if it is promoted by the boundary conditions.
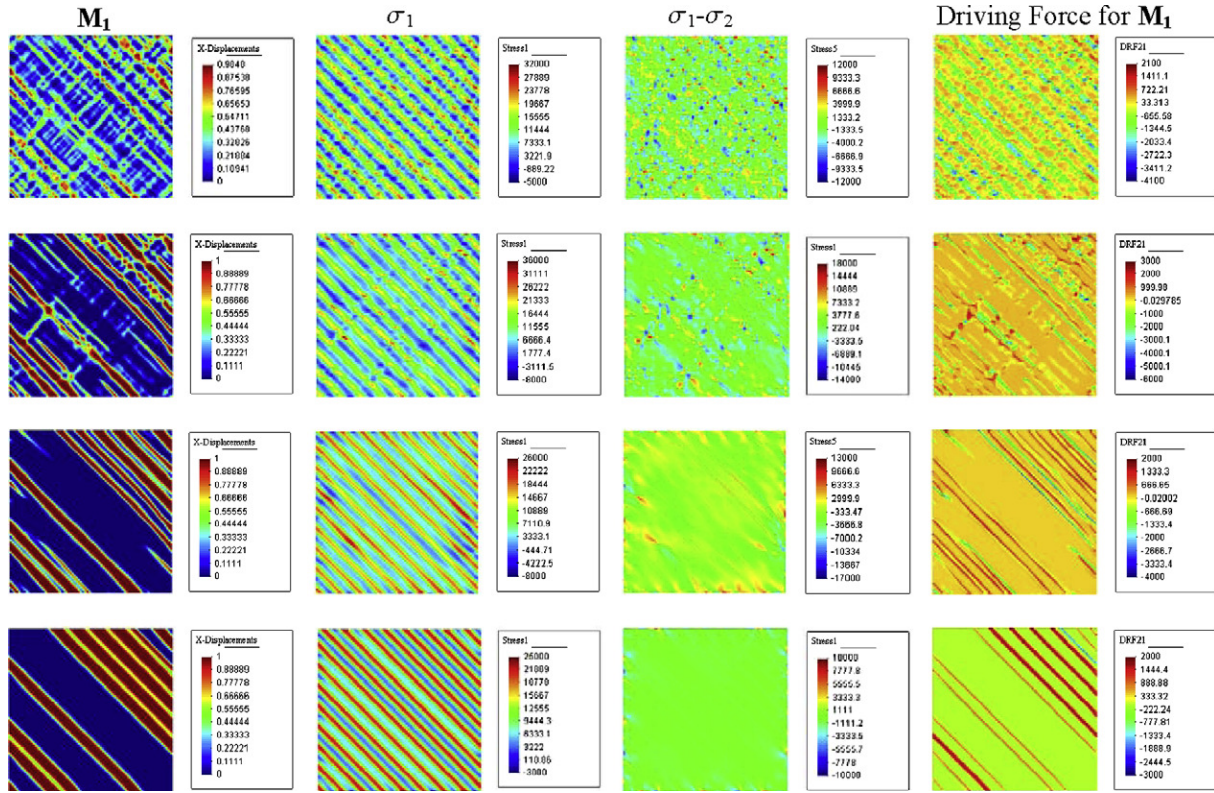
Fig. 18. Solution to the same problem as in Fig. 9 but with the periodic stress field $\sigma_{d1} = \sigma_{d2} = 10\,sin(8\pi(x+y))$; hence, $X^d_{1\to2} = 0$ and $X^d_{A\to M_i}$ is a periodic function along the diagonal. Left column: η_1; second and third columns: σ_1 and $\sigma_1 - \sigma_2$; right column: $\partial G/\partial \eta_1$, the local driving force for the evolution of η_1. The bottom row is the stationary solution (red is M_1 and blue is M_2). (For interpretation of the references to color in this figure legend, the reader is referred to the web version of this paper.)

We next considered a defect stress field that is stepped in both σ_{d1} and σ_{d2} with $\sigma_{d2} = -\sigma_{d1}$; the defect field $X^d_{1\to2} = 2\Delta\varepsilon_t\sigma_{d2}$ is plotted in Fig. 25. The stresses have the values 0 (green), -10 (yellow), and 10 GPa (blue). The system evolves into a four-grain microstructure in which many M_1 variants from one grain contact M_2 variants from other grains.

For the same initial and boundary conditions, we again used a stepped defect field satisfying $\sigma_{d2} = -\sigma_{d1}$, and $X^d_{1\to2} = 2\Delta\varepsilon_t\sigma_{d2}$, where the stresses assume the values 0 (green), -10 (yellow) and 10 GPa (blue), as shown in Fig. 26; the width of each step is $b = 0.2l$. The microstructure evolves unsymmetrically; the stationary microstructure consists primarily of rectangular lath and a few needle-like units (Fig. 26). Lath microstructures are usually observed when phase transformations are accompanied by plastic accommodation due to dislocation generation (Ghosh and Olson, 1994). Such a structure cannot appear in the absence of an athermal threshold because elastic energy minimization leads to relatively sharp tips. The widths of most (but not all) of the laths are determined by the defect stress field.

Finally, we carried out a simulation similar to the previous (Fig. 26) except that the step width was decreased to $b = 0.1l$. As seen in Fig. 27, the early stages of the microstructure evolution is similar to the evolution without defects (Fig. 10). However, the defect field arrests this complicated microstructure, which is a combination of four herring-bone microstructures.

In all of the above simulations with stepped $X^d_{1\to2}$, the initial stage of the evolution is heterogeneous nucleation of M_2 (M_1) units in the regions with positive (negative) $X^d_{1\to2}$. The late-time growth of martensitic units is driven by a reduction in the energy of the internal stress field.

Note that in Kartha et al. (1995), heterogeneous distributions of disorder and an elastic constant were used to model premartensitic structures like tweeds. In Abeyaratne et al. (1996), an oscillatory contribution was added to a local mesoscale potential in terms of the volume fraction of a martensitic variant, and this produces an athermal threshold for the mesoscale modeling, as in other mesoscale models (Ghosh and Olson, 1994; Levitas et al., 2004). This approach is not applicable to nanoscale phase field modeling because it arrests unphysical intermediate configurations.

8. Concluding remarks

In this paper, interface propagation kinetics was incorporated in advanced phase field models developed in Levitas and Preston (2002a,b) and Levitas et al. (2003). For 1D, we obtained and analyzed both analytical and numerical
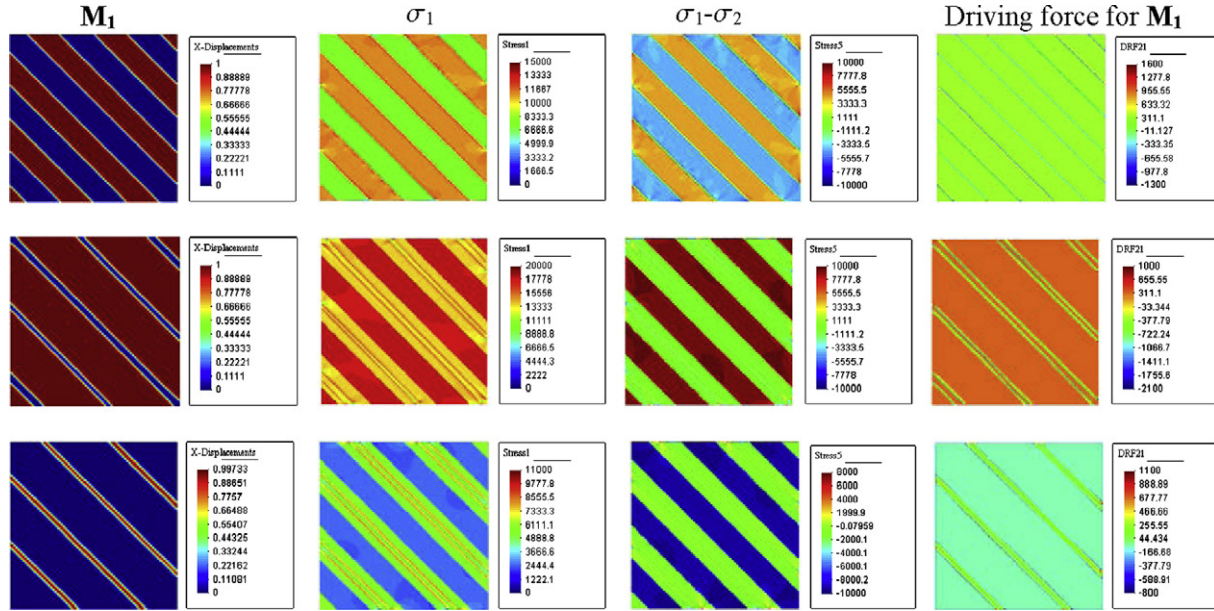
Fig. 19. (top row) Stationary solution following evolution from a stochastic initial state under $\sigma_{b1} = \sigma_{b2} = 10$ GPa in the presence of a plane square wave defect stress field (see text for details). The final state is a twinned microstructure with twins occupying adjacent regions of positive and negative $X^d_{1\rightarrow 2}$. (middle row) For $\sigma_{b1} = 15$ GPa and $\sigma_{b2} = 10$ GPa the driving force for the $M_2 \rightarrow M_1$ phase transformation exceeds the athermal threshold of 4 GPa and variant M_1 grows until the phase transformation is complete. (bottom row) Similarly, when $\sigma_{b1} = 10$ GPa and $\sigma_{b2} = 5$ GPa, so that the driving force for the $M_1 \rightarrow M_2$ phase transformation exceeds the athermal threshold, variant M_2 grows until the phase transformation is complete.
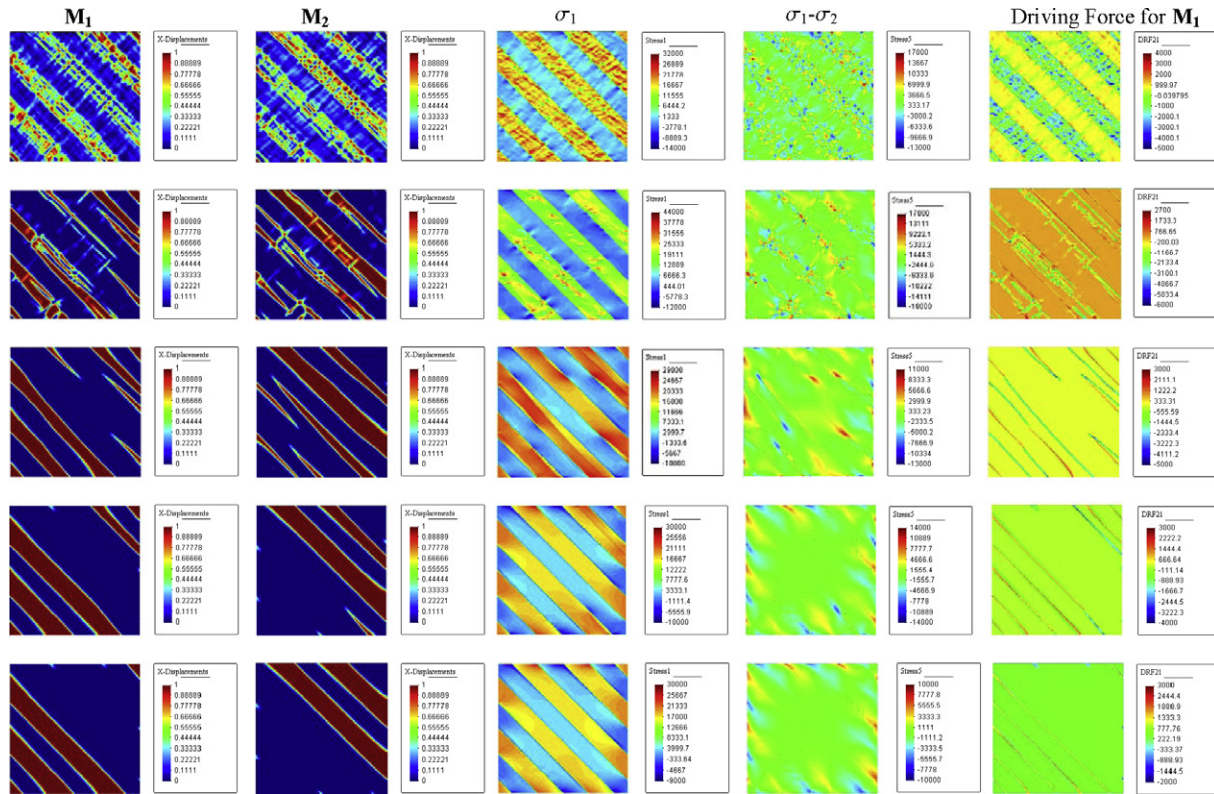
Fig. 20. Evolution of stochastic initial data under $\sigma_{b1} = \sigma_{b2} = 10$ GPa in the presence of a plane square wave defect stress field (see text for details). The stationary solution (last row) consists of M_i plates in the regions of positive stress separated by A plates in the regions of negative stress.
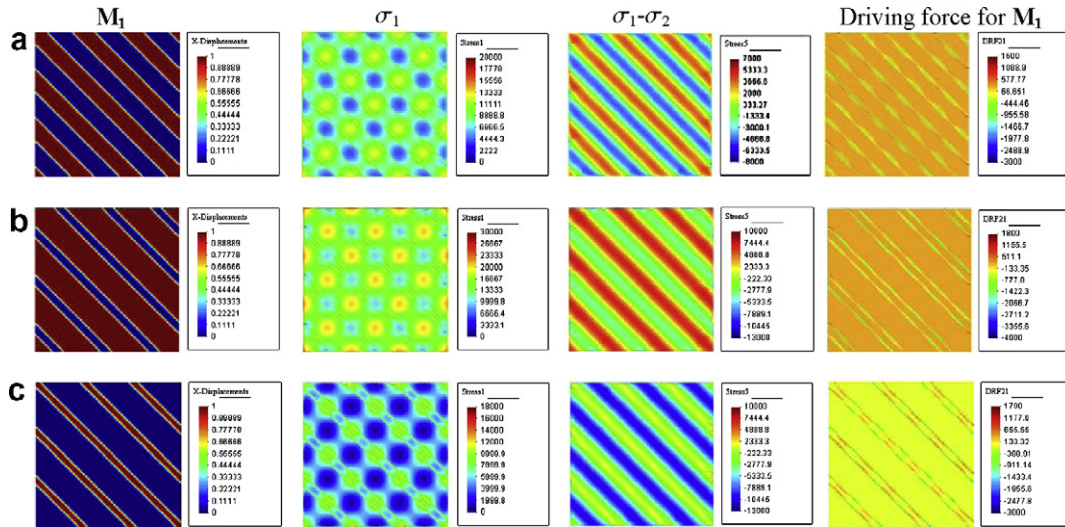
Fig. 21. (a) Stationary solution following evolution from stochastic initial data under $\sigma_{b1} = \sigma_{b2} = 10$ GPa in the presence of the periodic stress field $\sigma_{d1} = 5\cos(6\pi x)\cos(6\pi y)$ and $\sigma_{2d} = 5\sin(6\pi x)\sin(6\pi y)$ ($H = 5$ GPa); $X^d_{1-2} = -5\,\Delta\varepsilon_t\cos(6\pi(x+y))$. The solution converges to the same twinned microstructure as in Fig. 19 (top row). (b) Stationary microstructure for $\sigma_{b1} = 14$ GPa and $\sigma_{b2} = 10$ GPa. (c) Stationary microstructure for $\sigma_{b1} = 10$ GPa and $\sigma_{b2} = 6$ GPa. The stress–twin concentration is continuous and the slow cyclic stress–twin concentration curve *does not exhibit a hysteresis loop or energy dissipation.*
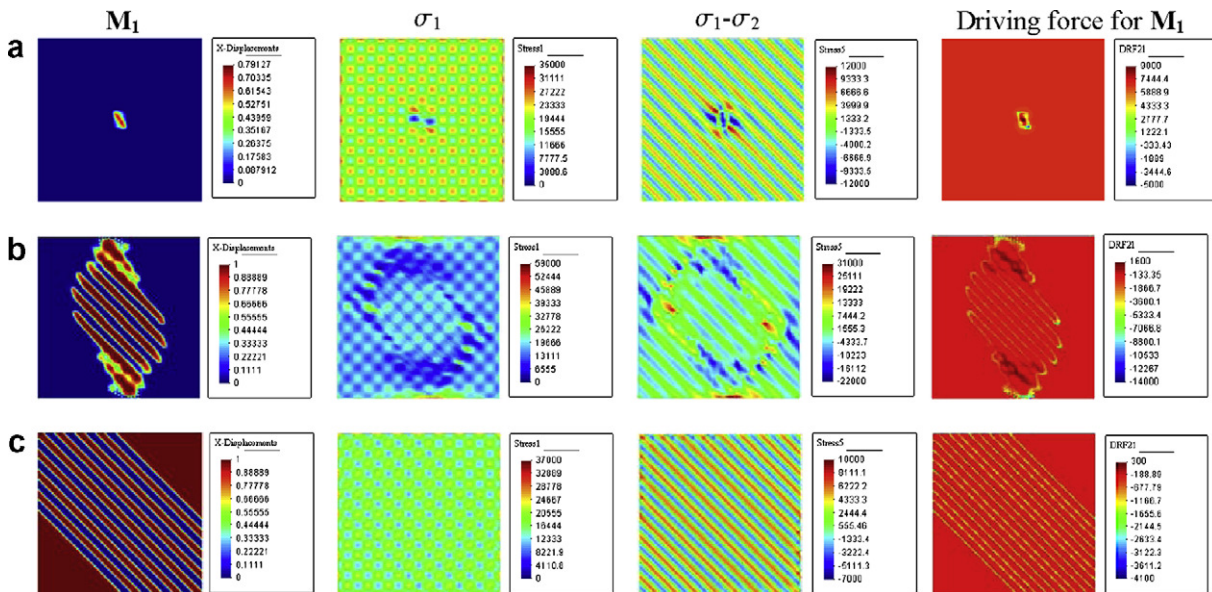
Fig. 22. Evolution of an embryo, $\eta_i = 0.1$, for $\sigma_{b1} = \sigma_{b2} = 15$ GPa, as in Fig. 10, but with the addition of the periodic defect field $\sigma_{d1} = 5\cos(16\pi x)\cos(16\pi y)$, $\sigma_{d2} = 5\sin(16\pi x)\sin(16\pi y)$. The stationary solution is a twinned microstructure (lowest row) with equal width twins, where M_2 – blue (M_1 – red) is located in the region with a positive (negative) X^d_{1-2}. Around two opposite corners, M_1 units evolve into triangles. (For interpretation of the references to color in this figure legend, the reader is referred to the web version of this paper.)

solutions of the *time-dependent* Ginzburg–Landau equations for A–M and M–M interface propagation. This included the determination of the interface velocity and profile, and a study of interface propagation instabilities for thermodynamic parameters near the conditions for lattice instability. In 2D, the coupled Ginzburg–Landau and quasi-static equations of linear elasticity were solved using FEM for the evolution of microstructures and stress fields in square samples.
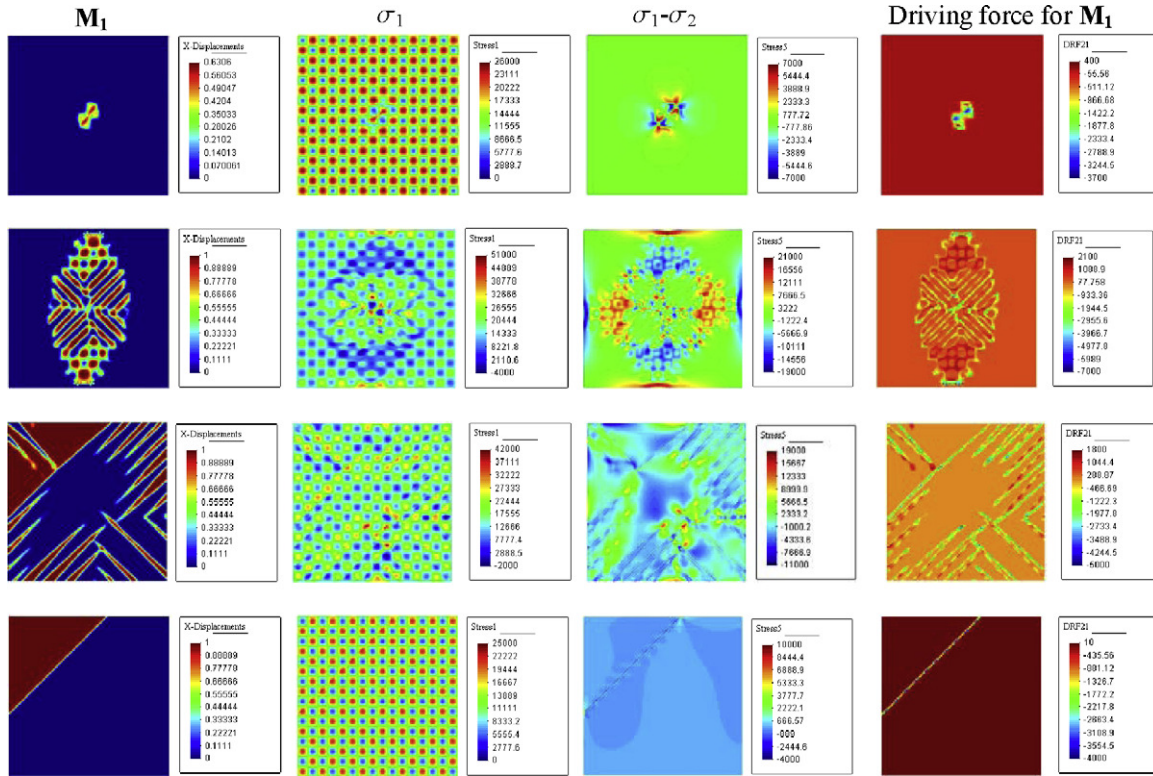
Fig. 23. Evolution of an embryo, $\eta_i = 0.1$, for $\sigma_{b1} = \sigma_{b2} = 15$ GPa (as in Figs. 10 and 22) but with the periodic field $\sigma_{d1} = \sigma_{d2} = 10\sin(16\pi x)\sin(16\pi y)$ ($X^d_{1\to2} = 0$). The intermediate microstructure consists of four twinned regions with clear boundaries between them. The final stationary solution is a two-twin microstructure.

We introduced an athermal threshold in the evolution equation for the order parameter and found that it works well in 1D, but this approach should be checked in higher dimensions.

We proposed the inclusion of oscillatory background stress fields in the phase field approach to model athermal thresholds to interface motion due to crystal defects. With these defect fields the system is arrested in experimentally observed microstructures instead of evolving to a single phase, and rate-independent stress and temperature hysteresis are present. In addition to producing an athermal threshold, these fields also create sites for heterogeneous nucleation. Some microstructures, e.g., laths, appear in phase field simulations with oscillatory defect fields that are not seen otherwise.

Similar results are obtained by introducing spatial oscillations in ΔG^θ due, for example, to fluctuations in chemical composition. An athermal threshold for twinning and dislocation motion can be introduced in the same way. For other types of phase transformations, oscillatory electric, magnetic, or other fields can be used. The oscillatory defect fields not only stabilize certain experimentally observed microstructures and cause rate-independent phase transformation hysteresis, but they also significantly change the microstructure.

Oscillatory defect fields not only open up new opportunities for realistic microstructure modeling, but also lead to a new major problem: how to find a realistic oscillatory field corresponding to a given defect structure. For any given (for example, experimentally observed) distribution of dislocations and other defects, we can find a numerically corresponding stress field σ^d using, for example, the approach in Wang et al. (2001). For any given (or evolving) heterogeneous alloy composition, in cases in which the dependence of ΔG^θ on the composition is known and included in the simulation, the heterogeneous (oscillatory) contribution to ΔG^θ appears automatically. For a particular defect stress field, the corresponding fields of the driving forces, $X^d_{A\to M}$ and $X^d_{M_i\to M_j}$, point to the possible effects of σ^d on the microstructure evolution. However, because the two traditional contributions to the driving force – the surface energy and the energy of the internal stress field due to the heterogeneous distribution of transformation strain – depend upon the evolving geometry of the martensitic units, the final microstructure may be very sensitive to variations in $X^d_{1\to2}$. This is typical of systems governed by material instability and may explain the variety of microstructures observed experimentally that do not follow from the minimization of the Ginzburg–Landau energy.

It is known that the defect microstructure and phase transformation hysteresis can be changed by thermomechanical treatment (Hornbogen, 1999); this can be modeled with oscillatory fields. In addition, if a phase transformation is
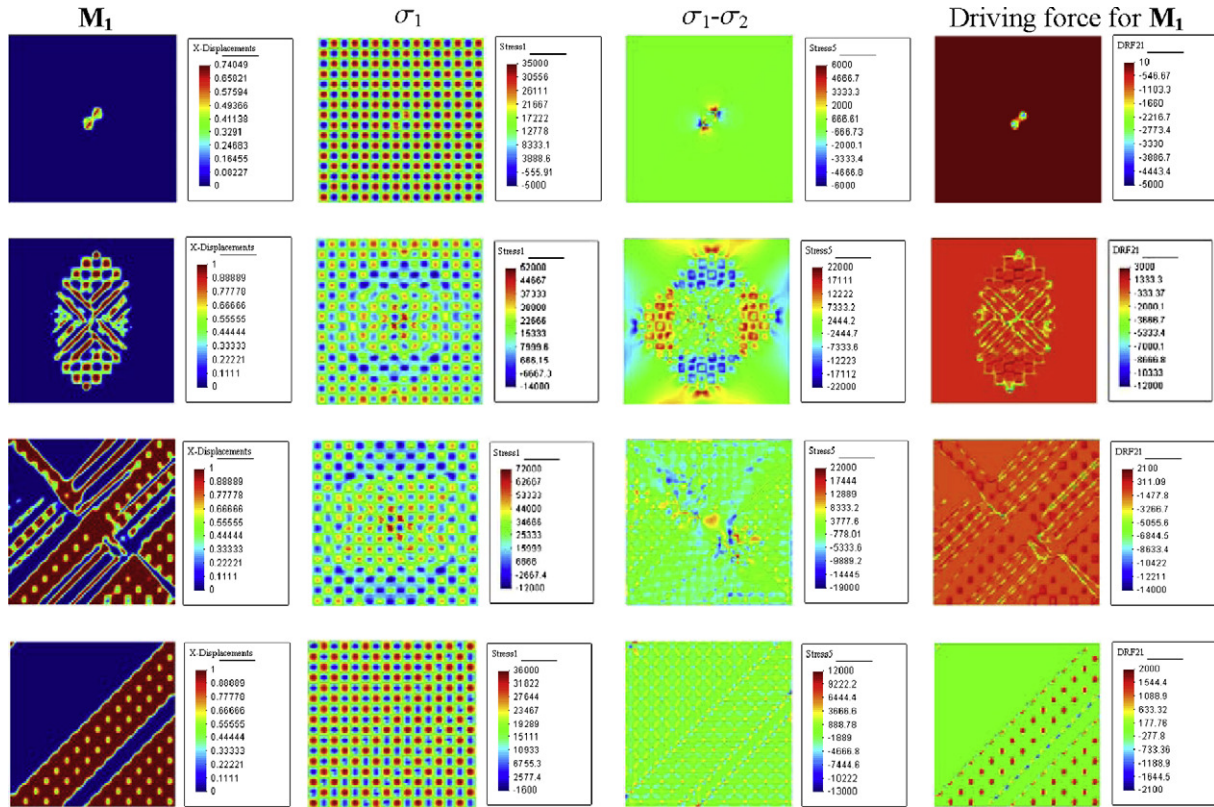
Fig. 24. Evolution of an embryo, $\eta_i = 0.1$, for $\sigma_{b1} = \sigma_{b2} = 15$ GPa (as in Fig. 23) but with the amplitude of the periodic field doubled: $\sigma_{d1} = \sigma_{d2} = 20\sin(16\pi x)\sin(16\pi y)$ ($X^d_{1\rightarrow2} = 0$). The stationary microstructure consists of four twins with islands of incompletely transformed material, which may serve as nucleation cites for another twin if promoted by the boundary conditions.
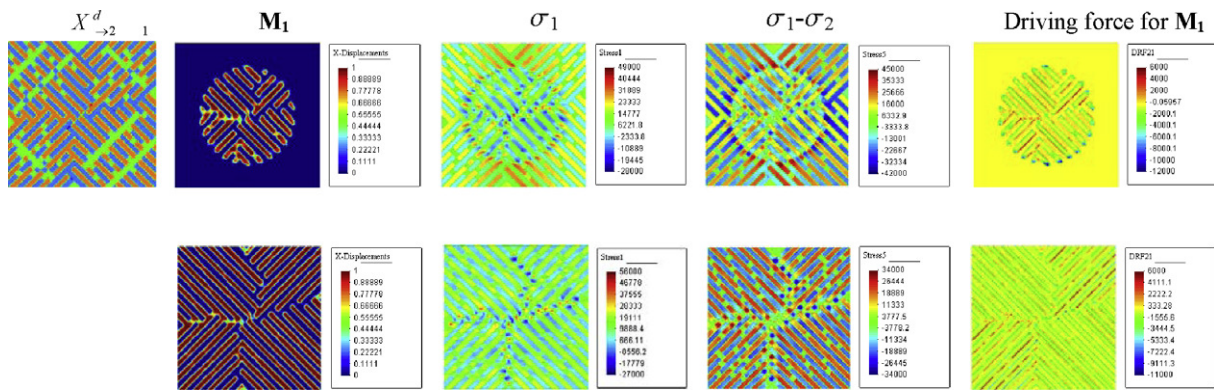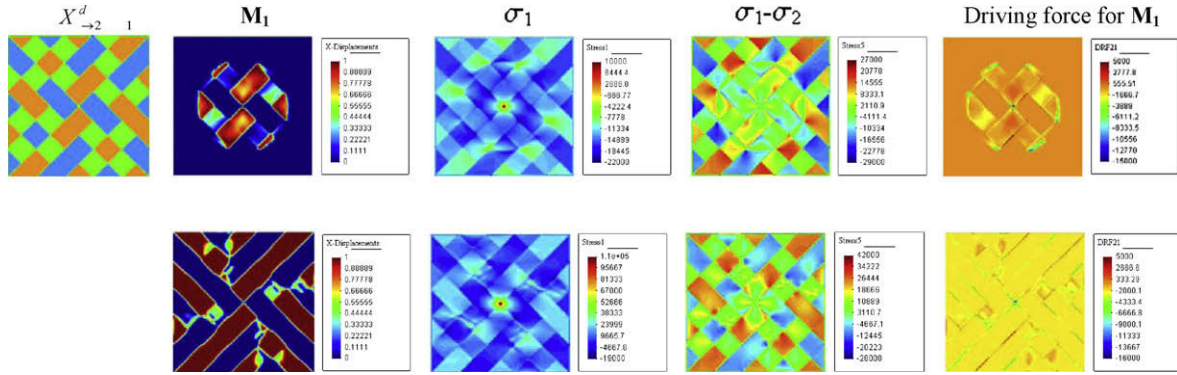

Fig. 25. Evolution of an embryo, $\eta_i = 0.1$, under $\sigma_{b1} = \sigma_{b2} = 15$ GPa (as in Fig. 24) but with a stepped defect stress field for which $\sigma_{d2} = -\sigma_{1d}$; $X^d_{1\rightarrow2} = 2\Delta\varepsilon_t\sigma_{d2}$ is shown top left. Stress values are 0 (green), −10 (yellow), and 10 GPa (blue). The stationary microstructure is shown in the last row. (For interpretation of the references to color in this figure legend, the reader is referred to the web version of this paper.)

accompanied by plastic accommodation, the defect structure changes, and the athermal threshold increases (Ghosh and Olson, 1994), thus one needs to determine the evolving oscillatory field. The numerical solution to this coupled defect field-phase structure problem, is, however, quite challenging.

In the future we will study oscillatory defect fields in the context of our phase field model for finite strain and material rotation (Levitas and Preston, 2005; Levitas et al., 2009).

Fig. 26. Evolution of an embryo, $\eta_i = 0.1$, under $\sigma_{b1} = \sigma_{b2} = 15$ GPa with a stepped defect field satisfying $\sigma_{d2} = -\sigma_{1d}$ and $X_{1 \rightarrow 2}^d = 2\Delta\varepsilon_t\sigma_{d2}$, as in Fig. 24, but with a different step distribution – compare $X_{1 \rightarrow 2}^d$ in this figure and Fig. 25. Stress values are 0 (green), −10 (yellow), and 10 GPa (blue). The last row shows the stationary microstructure, which consists mostly of rectangular laths and a few needle-like units. (For interpretation of the references to color in this figure legend, the reader is referred to the web version of this paper.)
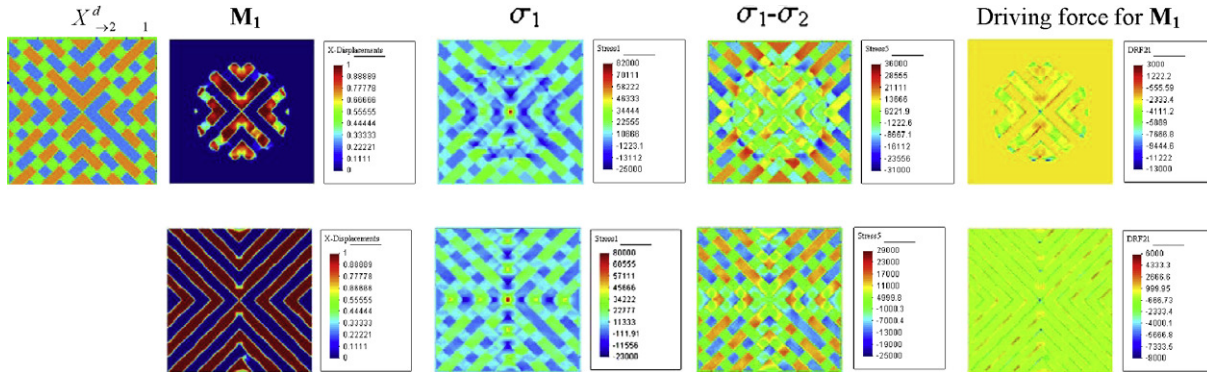
Fig. 27. Similar to Fig. 26 but with the step width reduced to $b = 0.1l$. Stress values are 0 (green), −10 (yellow), and 10 GPa (blue). The last row shows the stationary microstructure, which is a combination of four herring-bone microstructures. (For interpretation of the references to color in this figure legend, the reader is referred to the web version of this paper.)

Acknowledgements

References

Abeyaratne, R., Knowles, J.K., 1993. A continuum model of a thermoelastic solid capable of undergoing phase transitions. J. Mech. Phys. Solids 44, 541–571.
Abeyaratne, R., Chu, C., James, R.D., 1996. Kinetics of materials with wiggly energies: theory and application to the evolution of twinning microstructures in a Cu–Al–Ni shape memory alloy. Philos. Mag. A 73 (2), 457–497.
Ahluwalia, R., Lookman, T., Saxena, A., Bishop, A.R., 2003. Elastic deformation of polycrystals. Phys. Rev. Lett. 91, 055501.
Artemev, A., Jin, Y., Khachaturyan, A.G., 2001. Three-dimensional phase field model of proper martensitic transformation. Acta Mater. 49, 1165–1177.
Auricchio, F., Reali, A., Stefanelli, U., 2007. A three-dimensional model describing stress-induced solid phase transformation with permanent inelasticity. Int. J. Plast. 23, 207–226.
Bhattacharya, K., 2004. Microstructure of Martensite: Why It Forms and How It Gives Rise to the Shape-Memory Effect. Oxford University Press, Oxford.
Boyd, J.G., Lagoudas, D.C., 1996. A thermodynamical constitutive model for shape memory materials. Part I. The monolithic shape memory alloy. Int. J. Plast. 12, 805–842.
Curnoe, S.H., Jacobs, A.E., 2001a. Statics and dynamics of domain patterns in hexagonal–orthorhombic ferroelastics. Phys. Rev. B 63, 094110.
Curnoe, S.H., Jacobs, A.E., 2001b. Time evolution of tetragonal–orthorhombic ferroelastics. Phys. Rev. B 64, 064101.
Falk, F., 1983. Ginzburg–Landau theory of static domain walls in shape-memory alloys. Z. Phys. B: Condens. Matter 51, 177–185.
Ghosh, G., Olson, G.B., 1994. Kinetics of F.C.C. → B.C.C. heterogeneous martensitic nucleation. I. The critical driving force for athermal nucleation and II. Thermal activation. Acta Metall. Mater. 42 (10), 3361–3370. 3371–3379.
Grujicic, M., Olson, G.B., Owen, W.S., 1985. Mobility of martensitic interfaces. Metall. Trans. A, 1713–1722. 1723–1744.
Hornbogen, E.J., 1999. Ausforming of NiTi. J. Mater. Sci. 34 (3), 599–606.
Hu, S.Y., Li, Y.L., Zheng, Y.X., Chen, L.Q., 2004. Effect of solutes on dislocation motion – a phase-field simulation. Int. J. Plast. 20, 403–425.
Idesman, A.V., Levitas, V.I., Preston, D.L., Cho, J.-Y., 2005. Finite element simulations of martensitic phase transitions and microstructure based on strain softening model. J. Mech. Phys. Solids 53 (3), 495–523.

Idesman, A.V., Cho, J.-Y., Levitas, V.I., 2008. Finite element modeling of dynamics of martensitic phase transitions. Appl. Phys. Lett. 93, 043102.

Jacobs, A.E., Curnoe, S.H., Desai, R.C., 2003. Simulations of cubic–tetragonal ferroelastics. Phys. Rev. B 68, 224104.

Jin, Y.M., Artemev, A., Khachaturyan, A.G., 2001. Three-dimensional phase field model of low-symmetry martensitic transformation in polycrystal: simulation of ζ_2 martensite in AuCd alloys. Acta Mater. 49, 2309–2320.

Kartha, S., Krumhansl, J.A., Sethna, J.P., Wickham, L.K., 1995. Disorder-driven pretransitional tweed pattern in martensitic transformations. Phys. Rev. B 52, 803–822.

Kerr, W.C., Killough, M.G., Saxena, A., Swart, P.J., Bishop, A.R., 1999. Role of elastic compatibility in martensitic texture evolution. Phase Trans. 69, 1165–1177.

Kocks, U.F., Argon, A.S., Ashby, M.F., 1975. Thermodynamics and kinetics of slip. In: Chalmers, B., Christian, J.W., Massalski, T.B. (Eds.), Progress in Materials Science, vol. 19. Pergamon Press, Oxford.

Kondaurov, V.I., Nikitin, L.V., 1986. First order phase transitions in elastoviscoplastic medium. Mech. Solids 21, 130–139.

Kressea, O., Truskinovsky, L., 2003. Mobility of lattice defects: discrete and continuum approaches. J. Mech. Phys. Solids 51, 1305–1332.

Levitas, V.I., 1994. Thermomechanical description of pseudoelasticity – the threshold-type dissipative force with discrete memory. Mech. Res. Commun. 21, 273–280.

Levitas, V.I., 1995. Thermomechanics of martensitic phase-transitions in elastoplastic materials. Mech. Res. Commun. 22 (1), 87–94.

Levitas, V.I., 1997. Phase transitions in elastoplastic materials: continuum thermomechanical theory and examples of control. Part I and II. J. Mech. Phys. Solid 45 (6 and 7), 923–947. 1203–1222.

Levitas, V.I., 1998. Thermomechanical theory of martensitic phase transformations in inelastic materials. Int. J. Solids Struct. 35, 889–940.

Levitas, V.I., 2000a. Structural changes without stable intermediate state in inelastic material. Part I. General thermomechanical and kinetic approaches. Int. J. Plast. 16, 805–849.

Levitas, V.I., 2000b. Structural changes without stable intermediate state in inelastic material. Part II. Applications to displacive and diffusional-displacive phase transformations, strain-induced chemical reactions and ductile fracture. Int. J. Plast. 16, 851–892.

Levitas, V.I., 2004. High-pressure mechanochemistry: conceptual multiscale theory and interpretation of experiments. Phys. Rev. B 70 (18), 184118.

Levitas, V.I., Lee, D.-W., 2007. Athermal resistance to an interface motion in phase field theory of microstructure evolution. Phys. Rev. Lett. 99, 245701.

Levitas, V.I., Ozsoy, I.B., 2009a. Micromechanical modeling of stress-induced phase transformations. Part 1. Thermodynamics and kinetics of coupled interface propagation and reorientation. Int. J. Plast. 25, 239–280.

Levitas, V.I., Ozsoy, I.B., 2009b. Micromechanical modeling of stress-induced phase transformations. Part 2. Computational algorithms and examples. Int. J. Plast. 25, 546–583.

Levitas, V.I., Preston, D.L., 2002a. Three-dimensional Landau theory for multivariant stress-induced martensitic phase transformations. I. Austenite ↔ martensite. Phys. Rev. B 66, 134206.

Levitas, V.I., Preston, D.L., 2002b. Three-dimensional Landau theory for multivariant stress-induced martensitic phase transformations. II. Multivariant phase transformations and stress space analysis. Phys. Rev. B 66, 134207.

Levitas, V.I., Preston, D.L., 2005. Thermomechanical lattice instability and phase field theory of martensitic phase transformations, twinning and dislocations at large strains. Phys. Lett. A 343, 32–39.

Levitas, V.I., Idesman, A.V., Stein, E., 1999. Shape memory alloys: micromechanical modeling and numerical analysis of structures. J. Intell. Mater. Sys. Struct. 10 (12), 983–996.

Levitas, V.I., Idesman, A.V., Olson, G.B., Stein, E., 2002c. Numerical modeling of martensite growth in elastoplastic material. Philos. Mag. A 82 (3), 429–462.

Levitas, V.I., Preston, D.L., Lee, D.-W., 2003. Three-dimensional Landau theory for multivariant stress-induced martensitic phase transformations III. Alternative potentials, critical nuclei, kink solutions, and dislocation theory. Phys. Rev. B 68, 134201.

Levitas, V.I., Idesman, A.V., Preston, D.L., 2004. Microscale simulation of evolution of martensitic microstructure. Phys. Rev. Lett. 93, 105701.

Levitas, V.I., Preston, D.L., Lee, D.-W., 2006a. Ginzburg–Landau theory of microstructures: stability, transient dynamics, and functionally graded nanophases. Europhys. Lett. 75 (1), 84–90.

Levitas, V.I., Lee, D.-W., Preston, D.L., 2006b. Phase field theory of surface- and size-induced microstructures. Europhys. Lett. 76 (1), 81–87.

Levitas, V.I., Levin, V.A., Zingerman, K.M., Freiman, E.I., 2009. Displacive phase transitions at large strains: Phase-field theory and simulations. Phys. Rev. Lett. 103, 025702.

Lim, T.J., McDowell, D.L., 2002. Cyclic thermomechanical behavior of a polycrystalline pseudoelastic shape memory alloy. J. Mech. Phys. Solids 50 (3), 651–676.

Lookman, T., Shenoy, S.R., Rasmussen, K.Ø., Saxena, A., Bishop, A.R., 2003a. Ferroelastic dynamics and strain compatibility. Phys. Rev. B 67, 024114.

Lookman, T., Shenoy, S.R., Rasmussen, K.Ø., Saxena, A., Bishop, A.R., 2003b. On dynamics of ferroelastic transitions. J. Phys. IV: JP 112, 195–199.

Miracle, D.B., 1993. The physical and mechanical properties of NiAl. Acta Metall. Mater. 41 (3), 649–684.

Ngan, S.C., Truskinovsky, L., 1999. Thermal trapping and kinetics of martensitic phase boundaries. J. Mech. Phys. Solids 47, 141–172.

Olson, G.B., Cohen, M., 1986. Dislocation theory of martensitic transformations. In: Nabarro, F.R.N. (Ed.), Dislocations in Solids, vol. 7. North-Holland, Amsterdam. 295 pp., Chapter 37.

Pan, H., Thamburaja, P., Chau, F.S., 2007. Multi-axial behavior of shape-memory alloys undergoing martensitic reorientation and detwinning. Int. J. Plast. 23, 711–732.

Peng, X., Pi, W., Fan, J., 2008. A micro structure-based constitutive model for the pseudoelastic behavior of NiTi SMAs. Int. J. Plast. 24, 966–990.

Pitteri, M., Zanzotto, G., 2002. Continuum Models for Phase transitions and Twinning in Crystals. Chapman & Hall/CRC Press, London/Boca Raton, FL.

Rasmussen, K.Ø., Saxena, A., Bishop, A.R., Albers, R.C., Shenoy, S.R., 2001. Three-dimensional elastic compatibility and varieties of twins in martensites. Phys. Rev. Lett. 87 (5), 055704.

Salje, E.K., 1991. Phase Transitions in Ferroelastic and Co-Elastic Crystals: An Introduction for Mineralogists, Material Scientists and Psysicists. Cambridge University Press, Cambridge.

Seol, D.J., Hu, S.Y., Li, Y.L., Chen, L.Q., Oh, K.H., 2003. Cubic to tetragonal martensitic transformation in a thin film elastically constrained by a substrate. Met. Mater. Int. 9 (3), 221–226.

Shenoy, S.R., Lookman, T., Saxena, A., Bishop, A.R., 1999. Martensitic textures: multiscale consequences of elastic compatibility. Phys. Rev. B 60, R12537.

Thamburaja, P., Anand, L., 2002. Superelastic behavior in tension-torsion of an initially-textured Ti–Ni shape-memory alloy. Int. J. Plast. 18, 1607–1617.

Theil, F., Levitas, V.I., 2000. A study of a Hamiltonian model for phase transformations including microkinetic energy. Math. Mech. Solids 5 (3), 337–368.

Toledano, J.C., Toledano, P., 1987. The Landau Theory of Phase Transitions: Application to Structural, Incommensurate, Magnetic, and Liquid Crystal Systems. World Scientific, Singapore.

Valanis, K.C., 1996. A gradient theory of internal variables. Acta Mech. 116, 1–14.

Vedantam, S., 2006. Constitutive equations for rate-dependent pseudoelastic behaviour of shape memory alloys. Smart Mater. Struct. 15, 1172–1178.

Wang, Y., Khachaturyan, A.G., 1997. Three-dimensional field model and computer modeling of martensitic transformations. Acta Mater. 45 (2), 759–773.

Wang, Y.U., Jin, Y.M., Cuitino, A.M., Khachaturyan, A.G., 2001. Nanoscale phase field microelasticity theory of dislocations: model and 3D simulations. Acta Mater. 49, 1847–1857.

Zienkiewicz, O.C., Taylor, R.L., 2000. The Finite Element Method. Butterworth–Heinemann, Oxford.